Politécnica UFRJ

EXPERIMENTAL STUDY ON TAYLOR BUBBLES

Renato Rosa de Oliveira

Undergraduate Project submitted to the Mechanical Engineering Department of Escola Politécnica, Universidade Federal do Rio de Janeiro, as part of the requirements for obtaining the title of Mechanical Engineer.

Advisors: Gustavo Rabello dos Anjos
Cassiano Tecchio

Rio de Janeiro
February 2026

UNIVERSIDADE FEDERAL DO RIO DE JANEIRO

Escola Politécnica

Departamento de Engenharia Mecânica

EXPERIMENTAL STUDY ON TAYLOR BUBBLES

Renato Rosa de Oliveira

Undergraduate Project submitted to the Mechanical Engineering Department of Escola Politécnica, Universidade Federal do Rio de Janeiro, as part of the requirements for obtaining the title of Mechanical Engineer.

Approved by:

Prof. Gustavo Rabello dos Anjos, Ph.D

Prof. Cassiano Tecchio, Ph.D

Prof. Juliana Braga Rodrigues Loureiro, Ph.D.

Prof. Rorey Leon Thompson, Ph.D

RIO DE JANEIRO, RJ – BRAZIL

FEBRUARY 2026

Rosa de Oliveira, Renato

Experimental Study on Taylor Bubbles/ Renato Rosa de Oliveira. – Rio de Janeiro: UFRJ/Escola Politécnica, 2026.

XVI, 66 p.: il.; 29, 7cm.

Advisors: Gustavo Rabello dos Anjos

Cassiano Tecchio

Undergraduate Project de Graduação – UFRJ/ Escola Politécnica/ Mechanical Engineering Department, 2026.

Bibliography: p. 50 – 53.

1. Taylor Bubbles. 2. Two-Phase Flow. 3. Interferometry. I. Rabello dos Anjos, Gustavo *et al.*. II. Federal University of Rio de Janeiro, UFRJ, Curso de Engenharia Mecânica. III. Estudo Experimental em Bolhas de Taylor.

"Estamos cansados de saber que, nem na escola, nem nos livros onde mandam a gente estudar, não se fala da efetiva contribuição das classes populares, da mulher, do negro, do índio na nossa formação histórica e cultural. Na verdade, o que se faz é folclorizar todos eles." - Lélia González

"Medo de quase nada Hoje, eu, um homem formado Olho pra trás e vejo toda inconsequência do passado Mas me arrependo de quase nada Somos tão jovens pra ficar calados dentro dessa caixa" - Arthur de Jesus Leal.

"Que mundo errado que nos separou de nós Eu nunca soube reparar as estações Nessa de cê não poder parar Sem sentir ficar pra trás Uma temporada ou mais De desilusões Na luta pra ninguém silenciar nossa voz Voltamos a falar dos sonhos pelas manhãs A nossa terra fértil foi vencendo o concreto O nosso reflorestamento erguendo-se em fé" - Gabriel Linhares da Rocha

Acknowledgements

I would like to express my deepest gratitude to my parents, Maria and Renato, my sister Marcelle, and my entire family and friends for their unwavering support, patience, and encouragement throughout my academic journey. You were my foundation during the most challenging moments.

I am especially thankful to those who helped me during a particularly difficult and academically challenging time in France—particularly Aymane, Eric, Lara, Lucas, Maurício, Maxsuel, Oliver, Rezende, and Rufino.

My sincere thanks go to Dr. Zhiguo Zeng, who played a fundamental role in my Parcours Recherche and continues to be a profound inspiration to the researcher and professional I strive to become.

I am deeply grateful to the entire team at LE2H, CEA, where I had the privilege of carrying out my internship. Special appreciation goes to my advisor, Dr. Cassiano Tecchio, for his trust, mentorship, and the opportunity to grow under his guidance; to my co-advisor, Dr. Vadim Nikolayev, for his insightful scientific direction; to the Lab Chief, Dr. Benjamin Cariteau, for his support; and to Ph.D. candidate Nathan Berteloot, for his thorough review of this work and his constant readiness to help. I also extend my thanks to everyone at the lab for the enriching discussions, and to Dr. Marco Magnini for his valuable simulations and contributions.

I would also like to acknowledge my advisor in Brazil, Prof. Gustavo Rabello dos Anjos, for his guidance and for making this international cooperation possible.

My gratitude extends to the members of the Nucleus of Interdisciplinary Fluid Dynamics (NIDF)—especially Adão and Dayanne—for their assistance and friendship, and to Prof. Átila and Profa. Juliana for the opportunity to work alongside such a dedicated team.

I am sincerely grateful to Professors Thiago Ritto and Roney Thompson for

their support during the organization of the Fifth Week of Mechanical Engineering, and for their recommendation letters during my application to the double degree program.

I extend my heartfelt appreciation to Professors Marcos Miola, Jorge Henrique Craveiro, Nilson Tassi, and Anderson Stumpf for their recommendation letters, which were instrumental in my acceptance into the double degree program.

Last, but certainly not least, a special thank you to my friend Eduardo Paiva, whose outstanding TCC template simplified the academic journey not only for me but for thousands of other students.

Resumo do Projeto de Graduação apresentado à Escola Politécnica/UFRJ como parte dos requisitos necessários para a obtenção do grau de Engenheiro Mecânico

ESTUDO EXPERIMENTAL EM BOLHAS DE TAYLOR

Renato Rosa de Oliveira

February/2026

Orientadores: Gustavo Rabello dos Anjos
Cassiano Tecchio

Departamento: Engenharia Mecânica

Este trabalho apresenta um estudo experimental sobre a hidrodinâmica de bolhas de Taylor ascendentes em um minicanal retangular vertical com seção transversal de 2×5 mm, utilizando ar e água como fluidos de trabalho. Este regime de escoamento é de particular interesse para o gerenciamento térmico de Pequenos Reatores Modulares (SMRs) e dispositivos microeletrônicos, onde a estabilidade do filme líquido fino que envolve a bolha governa o desempenho da transferência de calor. O objetivo principal foi caracterizar a espessura do filme líquido e a velocidade da bolha sob condições adiabáticas, cobrindo números de Capilaridade (Ca) entre 10^{-4} e 10^{-3} e números de Reynolds (Re) variando de 80 a 600. Foi desenvolvida uma configuração de diagnóstico óptico sincronizado, combinando *shadowgraphy* de alta velocidade para capturar a cinemática macroscópica da bolha e interferometria de luz branca (espectrometria) para medir a espessura micrométrica do filme líquido com alta resolução temporal. A técnica interferométrica foi validada utilizando uma amostra de referência de Óxido de Índio-Estanho (ITO). Os resultados experimentais mostraram velocidades de bolha variando de 0,03 a 0,22 m/s e espessuras de filme entre 5,8 μm e 22,2 μm. As espessuras de filme medidas foram comparadas com correlações semi-empíricas estabelecidas para condutos circulares e não circulares. Os dados mostraram excelente concordância com a correlação proposta por

Magnini et al. (2022) para geometrias retangulares, demonstrando a influência significativa da drenagem pelos cantos e da razão de aspecto do canal na dinâmica do filme, efeitos não capturados por modelos clássicos de tubos circulares.

Palavras-chave: Bolhas de Taylor, Escoamento Bifásico, Minicanais Retangulares, Interferometria, Filme Líquido Fino.

Abstract of Undergraduate Project presented to POLI/UFRJ as a partial fulfillment of the requirements for the degree of Mechanical Engineering

EXPERIMENTAL STUDY ON TAYLOR BUBBLES

Renato Rosa de Oliveira

February/2026

Advisors: Gustavo Rabello dos Anjos
Cassiano Tecchio

Department: Mechanical Engineering

This work presents an experimental study on the hydrodynamics of Taylor bubbles rising in a vertical rectangular mini-channel with a cross-section of 2×5 mm, using air and water as working fluids. This flow regime is of particular interest for the thermal management of Small Modular Reactors (SMRs) and microelectronic devices, where the stability of the thin liquid film surrounding the bubble governs heat transfer performance. The primary objective was to characterize the liquid film thickness and bubble velocity under adiabatic conditions, covering Capillary numbers (Ca) between 10^{-4} and 10^{-3} and Reynolds numbers (Re) ranging from 80 to 600. A synchronized optical diagnostic setup was developed, combining high-speed shadowgraphy to capture macroscopic bubble kinematics and white-light interferometry (spectrometry) to measure the micrometric liquid film thickness with high temporal resolution. The interferometric technique was validated using a reference Indium Tin Oxide (ITO) sample. Experimental results showed bubble velocities ranging from 0.03 to 0.22 m/s and film thicknesses between 5.8 μm and 22.2 μm. The measured film thicknesses were compared against established semi-empirical correlations for circular and non-circular conduits. The data showed excellent agreement with the correlation proposed by Magnini et al. (2022) for rectangular geometries,

demonstrating the significant influence of corner drainage and channel aspect ratio on film dynamics, which are not captured by classical circular-tube models.

Keywords: Taylor Bubbles, Two-Phase Flow, Rectangular Mini-channels, Interferometry, Thin Liquid Film.

Contents

List of Figures

List of Tables

Chapter 1

Introduction

1.1 Motivation

Two-phase flows, particularly gas–liquid mixtures, exhibit a wide range of flow patterns such as bubbly, slug, churn, and annular flow (WHALLEY *et al.*, 1982; WHALLEY, 1987; DUKLER e TAITEL, 1986) as it can be seen at Fig 1.1 . Among these regimes, slug flow is characterized by elongated gas bubbles—commonly referred to as Taylor bubbles—that span almost the entire channel cross-section and are separated by liquid slugs (DAVIES e TAYLOR, 1950).

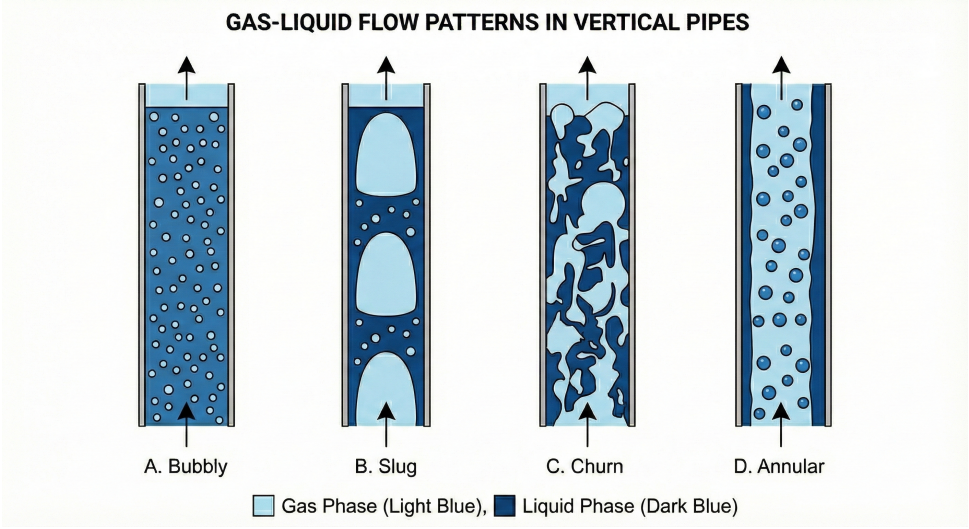

Figure 1.1: Illustration of typical gas–liquid two-phase flow regimes, including bubbly, slug, churn, and annular flow.

Taylor bubble flows are used in advanced thermal and chemical technologies due

to their unique transport characteristics. They are applied in chemical and biological reactors, as well as in cooling strategies for microelectronic devices (MEHTA e KHANDEKAR, 2014). Additionally, a recent review highlights their relevance in biomedical applications, pharmaceuticals, microreactors, and industrial process intensification (ETMINAN *et al.*, 2021). This widespread adoption underscores the versatility and engineering importance of slug-flow systems.

A fundamental advantage of slug flow in confined geometries lies in the enhancement of convective heat transfer relative to single-phase flows. The passage of elongated bubbles leaves a thin liquid film between the heated wall and the gas–liquid interface, which has low thermal resistance and acts as an efficient thermal bridge, while recirculation within the liquid slugs continually renews the wall-adjacent fluid and promotes rapid thermal homogenization (WALSH *et al.*, 2010). These mechanisms can increase the Nusselt number by up to an order of magnitude (WALSH *et al.*, 2010), enabling compact and efficient thermal components.

These benefits are of particular relevance for the development of Small Modular Reactors (SMRs), a promising evolution in nuclear power aimed at reducing capital costs and improving inherent safety. Due to their compact cores and passive cooling designs, SMRs require enhanced heat removal to sustain high power density while preventing thermal instabilities. Slug-flow-based cooling concepts, and specifically Taylor bubble motion in mini- and micro-channels, constitute a viable pathway toward this objective by improving heat transfer without imposing excessive pumping requirements.

However, the thermal-hydraulic performance of confined SMR evaporators is ultimately governed by the stability of the thin liquid film surrounding Taylor bubbles. When this micrometric film remains continuous, evaporative heat transfer is highly effective; conversely, film rupture or excessive thinning triggers localized dryout, severely degrading the heat transfer coefficient and potentially inducing thermal fatigue in the channel walls—a critical safety constraint for compact nuclear cores. Fig 1.2 illustrates this multiscale coupling: the left panel depicts a typical integral SMR power module (containment dimensions ≈23 m height, 4.6 m diameter); the right panel provides a magnification of a representative Printed Circuit Steam Generator (PCSG) channel (hydraulic diameter $D_h \approx$ 1.0–2.0 mm, active length

500–1000 mm)(CHO *et al.*, 2022). In this regime, the rising Taylor bubble is separated from the wall by a liquid film of 10–100 μm. The characteristic timescale for bubble passage in these high-velocity mini-channels is short, typically spanning less of a second (residence time $\mathcal{O}(0.5\text{ s})$), which allows for rapid phasic renewal while imposing strict limits on the allowable dryout frequency (KANG *et al.*, 2014).

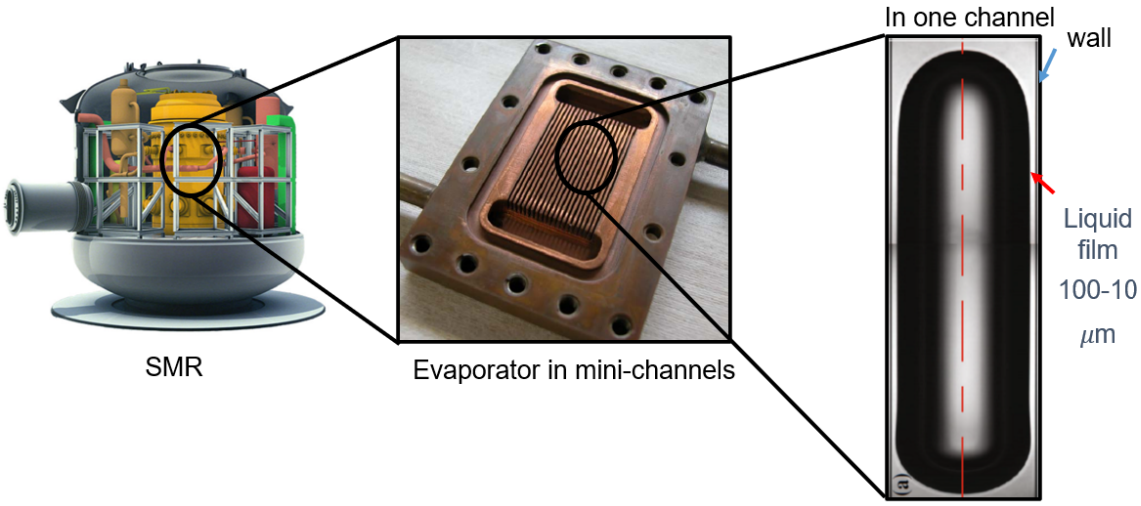

Figure 1.2: Illustration of how Taylor bubble flows in mini-channels are relevant for the cooling of Small Modular Reactors (SMRs). A micrometric liquid film surrounding a rising Taylor bubble governs local heat transfer and film stability within the evaporating channels.

As global energy systems move toward compact, passive, and low-carbon technologies, there is an increasing motivation to better understand and control the fluid dynamics of Taylor bubbles. The stability of the thin film, interfacial oscillations, and near-wall bubble physics must be accurately characterized to ensure safe and reliable operation. Beyond nuclear energy, these same challenges are crucial to next-generation electronics cooling, aerospace thermal control, and intensified chemical processing, where sustainability and efficiency are central drivers.

Research on confined slug flow has focused on characterizing bubble velocity (U_b) and liquid film thickness (h) as functions of key dimensionless groups. With r representing the hydraulic radius, the normalized film thickness h/r is most commonly correlated to the capillary number $Ca_b = \mu U_b/\sigma$, which quantifies the balance between viscous and surface tension forces. Additional corrections are often introduced to account for geometrical confinement and inertial contributions via the Reynolds

number.

1.2 State of the art

1.2.1 Circular Capillaries

In circular tubes, the liquid film surrounding a Taylor bubble is typically assumed to be azimuthally uniform, simplifying the analysis considerably. The foundational work of DAVIES e TAYLOR (1950) experimentally established that the amount of fluid bypassed by a bubble is a monotonically increasing function of the capillary number. Building on this observation, BRETHERTON (1961) developed a rigorous theoretical framework using lubrication theory to derive the asymptotic scaling law:

$$\frac{h}{R} = 1.34\, Ca_b^{2/3} \tag{1.1}$$

valid for the low-capillary regime ($Ca_b < 10^{-3}$), where viscous and surface tension forces dominate (BRETHERTON, 1961).

As bubble velocities increase, however, inertial effects become non-negligible and the film thickness deviates from this purely viscous limit. To address this, AUSSILLOUS e QUÉRÉ (2000) extended Bretherton's result by proposing an empirical correlation that accounts for the visco-inertial transition:

$$\frac{h}{R} = \frac{1.34\, Ca_b^{2/3}}{1 + 3.35\, Ca_b^{2/3}} \tag{1.2}$$

This expression captures the convergence of film thickness at higher capillary numbers due to geometric confinement. Furthermore, HAN e SHIKAZONO (2009) refined these models for micro-tubes, demonstrating that while Ca_b remains the primary governing parameter, the influence of the Reynolds number (Re) becomes increasingly important as the film thickens and inertial forces grow.

1.2.2 Rectangular Channels

The transition from circular to rectangular geometries introduces significant complexity due to the loss of axial symmetry. In rectangular capillaries, the liquid film is inherently non-uniform: capillary suction drives liquid accumulation in the channel corners, while the films on the flat walls remain considerably thinner (WONG

et al., 1995; MAGNINI, 2022). This corner accumulation creates bypass channels through which the liquid phase can flow around the bubble, a mechanism absent in circular tubes. The distribution of the liquid film is strongly influenced by the channel aspect ratio, which modulates both the corner meniscus geometry and the draining flows along the channel walls.

Compared to the extensive body of work on circular capillaries, studies addressing rectangular channels are relatively sparse. WONG *et al.* (1995) applied lubrication theory to polygonal capillaries in the asymptotic limit $Ca_b \to 0$, predicting that surface tension rearranges the liquid into static menisci of circular shape at the corners, connected by thin saddle-shaped films covering the channel walls. More recently, MAGNINI (2022) conducted systematic numerical simulations covering aspect ratios from 1 to 8 and capillary numbers spanning $0.005 \leq Ca_b \leq 0.5$. Their results showed that the centreline film thickness on the longer wall follows the scaling $h/R_h \approx 0.7\,Ca_b^{2/3}/(1+3.35\,Ca_b^{2/3})$, approximately half the value observed in circular tubes at the same conditions and remarkably independent of aspect ratio. They also identified inertia-driven undulations on the bubble interface near the rear meniscus when the Weber number exceeds a threshold value, phenomena not observed in purely viscous flows.

1.2.3 Recent Developments

Ongoing research has increasingly focused on the mechanics of the rear meniscus and the instability mechanisms associated with interfacial oscillations (ZHANG e NIKOLAYEV, 2021, 2022). A key parameter in characterizing these instabilities is the modified Weber number (We_p), which quantifies the competition between the destabilizing dynamic pressure force acting on the bubble rear and the stabilizing effect of surface tension. It is defined based on the relative velocity between the bubble and the liquid flow as:

$$We_p = \frac{\rho_l (U_b - U_l)^2 R}{\sigma} \tag{1.3}$$

where ρ_l is the liquid density and R is the characteristic radius. The identification of a critical modified Weber number linked to the onset of tail oscillations (ETMINAN *et al.*, 2021) underscores the need for accurate simultaneous measurement of U_b,

interface curvature, and h.

In the present work, adiabatic experiments were conducted in a rectangular vertical mini-channel using synchronized high-speed imaging and white-light interferometry with a fiber-coupled spectrometer. New reference data for film thickness, bubble velocity, and front meniscus curvature were obtained to address existing gaps in rectangular channel characterization.

1.3 Research Gap

Although extensive research has tried to characterize bubble velocity, shape, and fully developed film behavior, there is still limited experimental insight into the near-wall dynamics preceding film rupture and wall drying. In particular, recent observations suggest that localized interfacial oscillations in the rear region of Taylor bubbles may act as a triggering mechanism for film destabilization, yet this process remains insufficiently quantified experimentally.

Specifically, open questions remain regarding:

- film thickness determination over an extended range of Capillary numbers, including the influence of inertia and gravity,
- the onset conditions for film rupture in the presence of inertial perturbations,
- the role of rear-meniscus oscillations in destabilizing the liquid film,
- whether complete wall drying occurs or a residual nanometric film persists, and
- the motion of the contact line at the moment of rupture.

These mechanisms are schematically illustrated in Fig. 1.3, which highlights the coupling between rear-interface oscillations, thin-film deformation, and the initiation of local wall drying reported in previous experimental and conceptual studies (KHODAPARAST *et al.*, 2015; BORHANI *et al.*, 2010). The associated phenomena occur over micrometric spatial scales and millisecond time scales, requiring non-intrusive, high-precision optical diagnostics such as white-light interferometry to resolve the film thickness.

Addressing these knowledge gaps aligns with current international research efforts: Team Nottingham focuses on dryness triggering, while CEA/DRF/SPEC emphasizes drying conditions and contact-line physics.

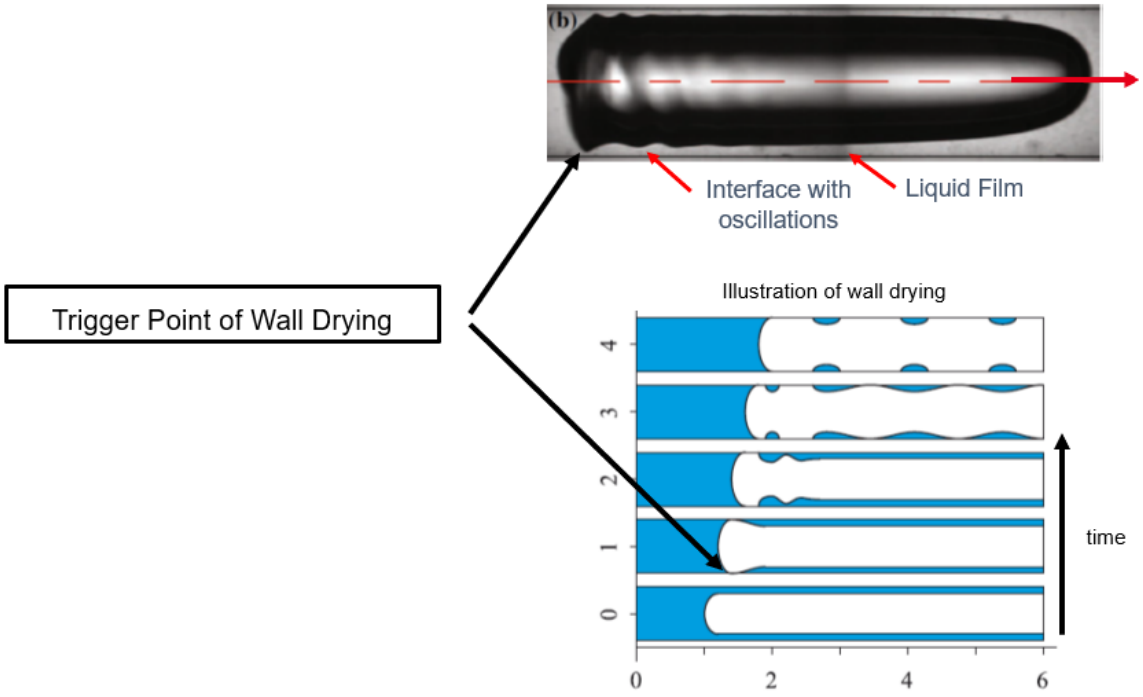

Figure 1.3: Illustration of near-wall dynamics in the rear region of a Taylor bubble. Oscillations of the rear interface can destabilize the thin liquid film, potentially triggering local wall drying and degrading heat transfer performance. Black and White image (KHODAPARAST *et al.*, 2015) Development to wall drying (BORHANI *et al.*, 2010)

1.4 Objectives

1.4.1 Scientific Objectives

- Measure bubble velocity, front meniscus curvature, and near-wall liquid film thickness in a vertical rectangular channel
- Provide high-precision experimental datasets to support physical modeling of film evolution in confined slug flows.

1.4.2 Industrial Objective

Contribute to the development of safer and more efficient compact heat-exchange systems for SMRs and other high heat-flux technologies.

Chapter 2

Bibliography Review

2.1 Modelling of the bubble

2.1.1 Problem definition and main equations

The problem is presented as follows: a gas bubble moves with a constant velocity **U** in a liquid of constant velocity **u** through a straight rectangular capillary initially filled with a wetting Newtonian liquid of viscosity μ and density ρ, while **g** is the gravitational acceleration. The gas phase has viscosity μ_g and density ρ_g, with a small viscosity ratio $\mu_g/\mu \ll 1$ for the air–liquid systems considered here. The interface between the gas and the liquid has a constant surface tension σ. The tube is thin enough, i.e. the characteristic length a (Radius of largest inscribed sphere of the capillary) is sufficiently small, so that the Reynolds and Bond numbers are both small and inertial and gravitational effects can be neglected in the liquid. In addition, because of the small viscosity ratio, the viscous stresses on the gas side of the interface are negligible compared to those in the liquid, so that the gas can be treated as effectively inviscid in the interfacial momentum balance.

The Reynolds (Re) number compares inertial forces to viscous forces:

$$Re = \frac{\rho U a}{\mu} \tag{2.1}$$

While Bond number (Bo), compares gravitational forces to surface tension forces:

$$Bo = \frac{\rho g a^2}{\gamma} \tag{2.2}$$

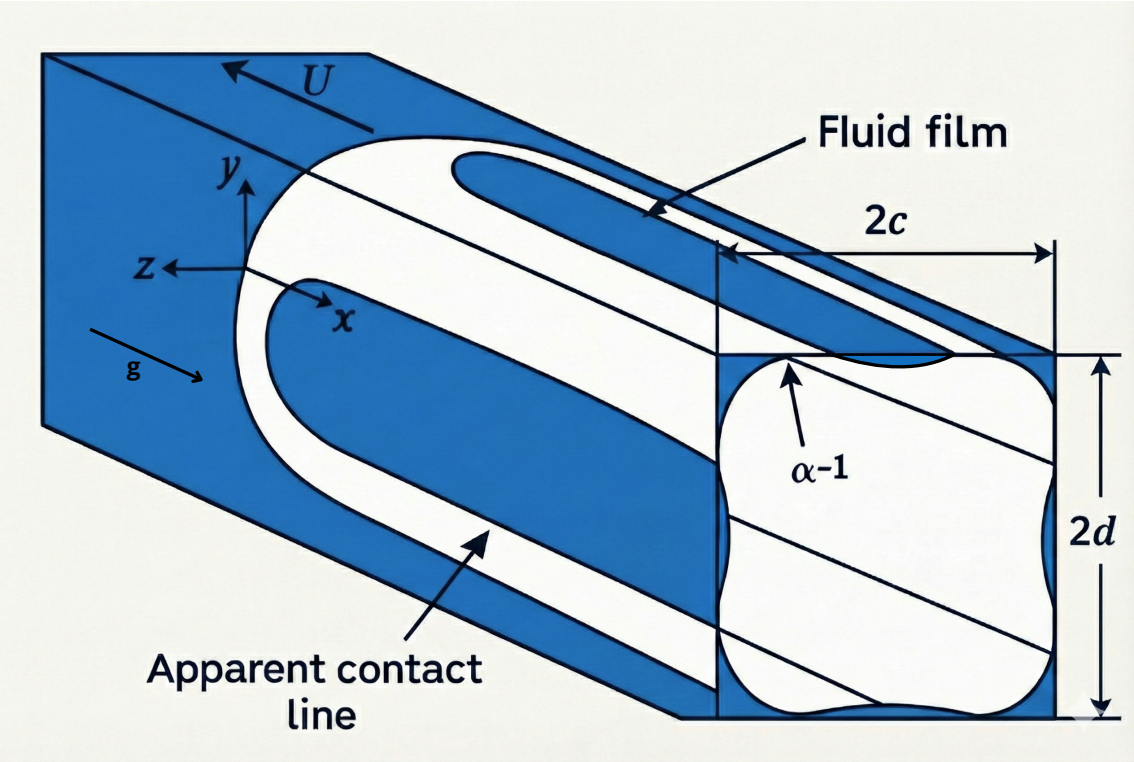

Figure 2.1: Taylor bubble flowing inside a capillary tube with dimensions 2c and 2d. The mean bubble curvature is α.

Because Reynold's number is low, the continuity and momentum equations correspond to Stoke's flow.

The continuity equation is:

$$\frac{\partial \rho}{\partial t} + \nabla \cdot (\rho \boldsymbol{u}) = 0 \tag{2.3}$$

For an incompressible fluid, it becomes:

$$\nabla \cdot \boldsymbol{u} = 0 \tag{2.4}$$

The momentum equation, for a Newtonian fluid is:

$$\rho \left(\frac{\partial \boldsymbol{u}}{\partial t} + \boldsymbol{u} \cdot \nabla \boldsymbol{u} \right) = -\nabla p + \mu \nabla^2 \boldsymbol{u} + \rho \boldsymbol{g} \tag{2.5}$$

In Stokes flow (or creeping flow), we make the following assumption:

- **Negligible inertial forces**: The Reynolds number is very small, so both the transient $\frac{\partial \boldsymbol{u}}{\partial t}$ and the convective term $\boldsymbol{u} \cdot \nabla \boldsymbol{u}$ can be neglected.

Since we are also neglecting gravitational forces, the respective term $\rho \boldsymbol{g}$ is not taken into account. The simplified momentum equation then becomes:

$$\boldsymbol{\nabla} p = \mu \boldsymbol{\nabla^2 u}. \tag{2.6}$$

The coordinates are defined at the front of the bubble, with the x-axis pointing downstream, as shown in Figure 2.1. Lengths, velocity, pressure, and force are made dimensionless using a, U, σ/a, and $a\sigma$, respectively.

To derive the dimensionless equations, we'll use the following quantities

- $U[m/s]$ - Bubble's velocity used as characteristic quantity
- $\sigma/a[N/m^2]$ - Characteristic pressure scale associated with capillary pressure at the interface
- $a\sigma[N]$ - Characteristic force scale associated with surface-tension forces acting over a length α
- $\boldsymbol{u'} = \boldsymbol{u} + \boldsymbol{Ui}$ - This is the liquid velocity in the reference frame moving with the bubble,

Let (x, u', p, f) $[m, m/s, N/m^2, N]$ be the old variables and its respective unities. The new dimensionless variables are:

$$\widetilde{x} = \frac{x}{a},\ \widetilde{\boldsymbol{u}} = \frac{\boldsymbol{u'}}{U},\ \widetilde{p} = \frac{p}{\sigma/a}; \widetilde{f} = \frac{f}{a\sigma}$$

The dimensionless continuity and momentum equations are given by:

$$\widetilde{\boldsymbol{\nabla}} \cdot \widetilde{\boldsymbol{u}} = 0. \tag{2.7}$$

$$\widetilde{\boldsymbol{\nabla}} \widetilde{p} = Ca \widetilde{\boldsymbol{\nabla}}^{\boldsymbol{2}} \widetilde{\boldsymbol{u}}. \tag{2.8}$$

where $\widetilde{\nabla} = \boldsymbol{i}\frac{\partial}{a\partial\tilde{x}} + \boldsymbol{j}\frac{\partial}{a\partial\tilde{y}} + \boldsymbol{k}\frac{\partial}{a\partial\tilde{z}}$, p is the fluid pressure, $Ca = \frac{\mu U}{\sigma}$ is the capillary number, and $\widetilde{\mathbf{u}} = u\boldsymbol{i} + v\boldsymbol{j} + w\boldsymbol{k}$ represents the fluid velocity.

On the wall, the no-slip condition is expressed as:

$$\tilde{\boldsymbol{u}} = \boldsymbol{i}. \tag{2.9}$$

The motion is considered steady in the frame of reference that is moving at constant speed. Consequently, the bubble's surface acts as a stream surface, leading to the condition at the gas/liquid interface:

$$\boldsymbol{n} \cdot \tilde{\boldsymbol{u}} = 0. \tag{2.10}$$

At the interface, the stress boundary condition can be written as:

$$(-\tilde{p}\overline{\boldsymbol{I}} + 2Ca\overline{\boldsymbol{E}}) \cdot \boldsymbol{n} = \boldsymbol{n}\tilde{\boldsymbol{\nabla}} \cdot \boldsymbol{n}. \tag{2.11}$$

In this context, $\overline{\boldsymbol{I}}$ denotes the identity tensor, $\overline{\boldsymbol{E}}$ represents the strain rate tensor, $\boldsymbol{n}$ is the unit normal vector to the gas/liquid interface directed from the gas phase towards the liquid phase, and $\tilde{\boldsymbol{\nabla}} \cdot \boldsymbol{n}$ signifies the mean curvature of the interface (WEATHERBURN, 1938)

2.1.2 Regions of the Taylor Bubble Profile

Given the governing equations and boundary conditions established above, the bubble profile in the limit Ca $\to 0$ can be divided into two distinct regions. Following Bretherton (1961), the bubble-liquid interface separates into an *outer region* where surface tension dominates, and an *inner region* near the wall where both surface tension and viscous forces are important.

Outer Region: The Static Meniscus

In this section, we will derive α as a function of B, which is defined as the ratio of the rectangle's sides 2d/2c beind $d > c$

In the outer region, away from the tube wall, the viscous stresses are $O(\mu U/a)$, which are negligible compared to surface tension stresses $O(\sigma/a)$ when Ca $\to 0$. Consequently, the dimensionless momentum Eq.(2.7) reduces to:

$$\tilde{\nabla}\tilde{p} \approx 0, \tag{2.12}$$

implying uniform pressure in this region. The stress boundary condition (1.11) then simplifies to:

$$\tilde{\nabla} \cdot \mathbf{n} = -\tilde{p} \tag{2.13}$$

This is the equation of a surface of constant mean curvature. From geometric definiton we know that

$$\tilde{\nabla} \cdot \mathbf{n} = \alpha \tag{2.14}$$

where α is the mean curvature of the surface as represented in Fig. 1.1. And it is this last equation that governs the bubble shape.

Deriving an expression for α

In order to obtain an expression for α, the 2D version of Gauss' Theorem is used over a portion of the bubble far from the meniscus. Now, to reduce the dimensionality of the problem from 3D to 2D, we make the assumption that the vector field is symmetric and uniform in the x-direction. The meniscus far away from the nose reduces to circular arcs with radius $1/\alpha$, and thus the derivative with respect to x vanishes. Therefore, we have:

$$\widetilde{\boldsymbol{\nabla}} \cdot \boldsymbol{F} = \frac{\partial n_x}{a\partial \tilde{x}} + \frac{\partial n_y}{a\partial \tilde{y}} + \frac{\partial n_z}{a\partial \tilde{z}} \quad \Rightarrow \quad \widetilde{\boldsymbol{\nabla}} \cdot \boldsymbol{F} \approx \frac{\partial n_y}{a\partial \tilde{y}} + \frac{\partial n_z}{a\partial \tilde{z}} \tag{2.15}$$

$$\iiint_V (\widetilde{\boldsymbol{\nabla}} \cdot \boldsymbol{F})\, dx\, dy\, dz = \oiint_S (\boldsymbol{F} \cdot \boldsymbol{n})\, ds \tag{2.16}$$

where:

- V is the 3D volume,
- S is the boundary surface of the volume V,
- F is a vector field.

At this point, we are effectively considering a 2D problem in the y-z plane. Thus, we can now apply the 2D version of the divergence theorem. The surface integral in 3D over the volume V is now reduced to a surface integral over an area A, and the surface integral over the boundary S is reduced to a line integral over the boundary curve L:

$$\iint_A (\widetilde{\boldsymbol{\nabla}} \cdot \boldsymbol{n})\, dy\, dz = \oint_L (\boldsymbol{n} \cdot \boldsymbol{n})\, dl \tag{2.17}$$

where:

- A is the 2D area in the y-z plane,
- L is the boundary curve of the area A,
- dl is the differential element along the curve L.

By assuming symmetry in one direction and applying the divergence theorem in 2D, we have reduced the original 3D volume integral to a 2D surface integral, and finally to a line integral around the boundary of the 2D area.

From equation 2.14, we have

$$\iint_A \alpha \, dy \, dz = \oint_L (\boldsymbol{n} \cdot \boldsymbol{n}) \, dl \tag{2.18}$$

Since α is constant and we are integrating over a projection of the meniscus, the surface integral, LHS (left-hand side) of Eq. (2.18) becomes:

$$\alpha \iint_A dy \, dz = \alpha A \tag{2.19}$$

where A is the 2D area of the cross-section in the y-z plane.

The RHS (right-hand side) of Eq.(2.18) is a line integral around the boundary curve L. This integral represents the total boundary length, which is the perimeter L of the cross-sectional area:

$$\oint_L (\boldsymbol{n} \cdot \boldsymbol{n}) \, dl = L \tag{2.20}$$

Now, Eq.(2.18) can be written in the following manner:

$$\alpha A = L \tag{2.21}$$

The value of α depends on the geometry of the bubble, particularly the curvature of the arcs.

The calculation of α as a function of B (ratio of $2d/2c$) is as follows:

$$A = \underbrace{2B.2}_{\text{Total area of the cross-section}} - \underbrace{4[(\alpha^{-2}) - \frac{1}{4}\pi(\alpha^{-1})^2]}_{\text{Area occupied by the liquid}}$$

While L is calculated in this manner:

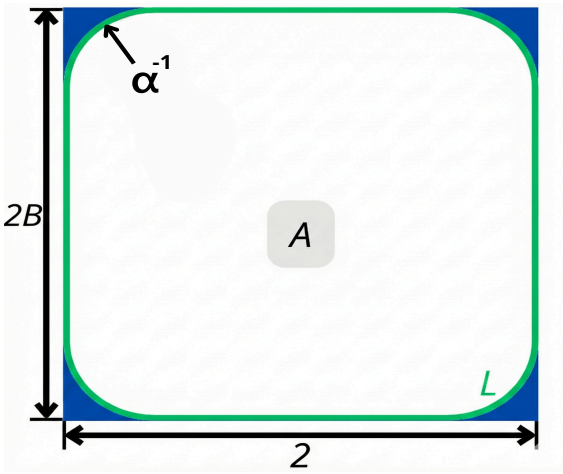

Figure 2.2: Rectangle sides now represented by 2 and 2B

$$L = \underbrace{4\frac{1}{4}(2\pi\alpha^{-1})}_{\text{perimeter of the curved corners}} + \underbrace{2[2(B-\alpha^{-1})+2(1-\alpha^{-1})}_{\text{sides of rectangle}}$$

Using Eq. (2.21) we arrive at the following expression:

$$B\alpha^2 - (B+1)\alpha - \frac{\pi}{4} + 1 = 0 \tag{2.22}$$

Which results in

$$\alpha = \frac{B+1+\sqrt{((B-1)^2+B\pi)}}{2B} \tag{2.23}$$

The other solution of the second degree equation is discarded because α should be bigger than 1 and B is also bigger than 1 by definition.

Inner Region: The Thin Film

In the inner region near the wall, the film thickness is much smaller than the characteristic length a, and the interface is nearly parallel to the wall. Under these conditions, both viscous and capillary forces become important and of the same order. Following the lubrication approximation framework of WONG *et al.* (1995), the governing equation for the film thickness $h(x,z)$ in the moving reference frame is

$$\frac{\partial h}{\partial x} + \frac{1}{3Ca}\nabla\cdot\left(h^3\,\nabla\nabla^2 h\right) = 0, \tag{2.24}$$

where $\nabla = \mathbf{i}\,\partial/\partial x + \mathbf{k}\,\partial/\partial z$ operates in the (x, z)-plane. The first term describes advection of film thickness by the bubble motion, while the second term represents capillary-driven redistribution of liquid within the film, with the capillary pressure given by the Laplace equation $p = -\nabla^2 h$.

The lubrication approximation is applicable in the inner region and the transition region under the following assumptions:

- The film is thin: $h/a \ll 1$.
- The interface slope is small: $|\partial h/\partial x| \ll 1$.
- Inertial effects remain negligible ($\mathrm{Re} \ll 1$).

Although the full inner solution of Eq. (2.24) reveals a sequence of six subregions along the downstream direction (WONG *et al.*, 1995), the present study primarily focuses on the *film deposition region*—the viscous–capillary transition zone of axial extent $O(a\,Ca^{1/3})$ adjacent to the rear meniscus—because the dynamics in this region determine the uniform film thickness h_∞ observed throughout the extended thin-film region along the bubble body, away from both the nose and tail caps.

In the deposition region, viscous stresses induced by the bubble motion balance capillary pressure gradients over the axial length scale (WONG *et al.*, 1995)

$$x \sim a\,Ca^{1/3},$$

where a is the characteristic transverse length scale of the channel. This yields the classical Bretherton-type (BRETHERTON, 1961) scaling for the deposited film thickness

$$h_\infty \sim a\,Ca^{2/3}.$$

Downstream of the deposition region, surface tension drives lateral redistribution within the deposited film, forming a parabolic cross-sectional profile over $x \sim a\,Ca^{-1}$ and subsequent drainage toward the corners over still longer scales ($x \gtrsim a\,Ca^{-1}$) (WONG *et al.*, 1995). For bubble lengths typical of Taylor bubble experiments, these rearrangement processes do not alter the leading-order $Ca^{2/3}$ thickness scaling imposed by deposition.

Accordingly, the $Ca^{2/3}$ scaling established in the deposition region provides the dominant control on the thin-film thickness throughout the extended thin-film region

along the bubble body and forms the basis for comparison with classical and recent correlations (WONG *et al.*, 1995) (MAGNINI *et al.*, 2022).

Transition: Parabolic profile and asymptotic matching

There is a transition between the hemispherical meniscus and the uniform thin film where both viscous and capillary forces are important. In this region, the interface profile must smoothly connect the constant-curvature meniscus to the thin film.

Under the assumptions of the lubrication approximation mentioned before, the Stokes momentum Eq.(2.6) is integrated across the film thickness, and applying the no-slip boundary condition in Eq.(2.9) and zero tangential stress at the interface yields the interface profile ODE:

$$\frac{d^3 y_1}{dx^3} = \frac{3\mu U}{\sigma} \frac{y_1 - h_\infty}{y_1^3}, \tag{2.25}$$

where $y_1(x)$ is the radial position of the interface and h_∞ is the film thickness far from the meniscus. Introducing dimensionless variables $\eta = y_1/h_\infty$ and $\xi = x/[h_\infty(3\mathrm{Ca})^{-1/3}]$, this becomes:

$$\frac{d^3\eta}{d\xi^3} = \frac{\eta - 1}{\eta^3}. \tag{2.26}$$

The asymptotic matching procedure connects the solution of the ODE to those of the inner (film) and outer (meniscus).

- **Near the meniscus** ($\eta \gg 1$): The equation simplifies to $d^3\eta/d\xi^3 \approx 0$, which integrates to a *parabolic profile*:

$$\eta(\xi) \approx \frac{1}{2} P\xi^2 + Q\xi + R. \tag{2.27}$$

  The constants P, Q, R are numerically determined by matching the curvature of the hemispherical meniscus.

- **Near the thin film** ($\eta \to 1$): The solution must approach the uniform film with $\eta = 1$ and $d\eta/d\xi = 0$, consistent with the zero contact angle assumption.

2.1.3 Reference studies and expected regimes

To contextualize the expected trends observed in the results, it is essential to clearly define the experimental and numerical conditions explored in the three main reference studies. The summaries below emphasize the relevant ranges of dimensionless numbers and the fluid properties employed in each work.

Visco-capillary to visco-inertial transition (AUSSILLOUS e QUÉRÉ, 2000)

Aussillous and Quéré investigated the onset of inertial effects in liquid film deposition by long bubbles in circular capillaries. Experiments were conducted in transparent polymeric tubes with radii $r = 0.42$, 0.62, 0.78, and 1.46 mm. The capillary number spanned a wide range, from $Ca \sim 10^{-2}$ up to values exceeding unity, reaching approximately $Ca \simeq 1.4$.

Low surface tension liquids ($\sigma \approx 20$ mN/m) were selected to enable high bubble velocities, including silicone oils with viscosities $\eta = 0.52$, 2.6, and 531 mPa s, ethanol ($\eta = 1.17$ mPa s), and alkanes such as heptane ($\eta = 0.42$ mPa s). A key outcome of this study was the identification of a visco-inertial regime in which the deposited film thickness exceeds the classical Taylor–Bretherton prediction. The critical capillary number for inertial thickening, Ca^*, was shown to decrease with increasing tube radius, highlighting the growing role of inertia at larger length scales.

Micro-scale inertial effects and Reynolds number dependence (HAN e SHIKAZONO, 2009)

Han and Shikazono performed high-resolution measurements of local liquid film thickness in micro-scale circular tubes made of Pyrex glass, with inner diameters $D = 0.3$, 0.5, 0.7, 1.0, and 1.3 mm. The explored capillary number range depended on the working fluid: for FC-40 and ethanol, experiments extended up to $Ca \approx 0.15$, while for water the maximum investigated value was $Ca \approx 0.12$.

The Reynolds number covered a broad interval, from $Re \approx 0$ up to $Re \sim 2000$. For $Re \gtrsim 2000$, the liquid film thickness was observed to become nearly insensitive to further increases in inertia, which was attributed to the transition from laminar to turbulent flow in the liquid phase. By employing fluids with markedly different densities and viscosities (water, ethanol, and FC-40), the authors isolated inertial

contributions and demonstrated that, at sufficiently large Ca, the dimensionless film thickness δ_0/D exhibits a minimum as a function of Re before increasing again. This non-monotonic behavior represents a clear deviation from purely visco-capillary models.

Geometric effects and three-dimensional drainage (MAGNINI *et al.*, 2022)

Magnini et al. studied long bubble propagation in square/rectangular capillaries with aspect ratios $\epsilon = 1$–8, covering Ca = 0.005–1 and Re = 1–1000.

In rectangular channels ($\epsilon > 1$), the film is asymmetric: thicker on the short wall, saddle-shaped with a dimple on the long wall. Unlike circular tubes, the film thins continuously toward the bubble rear due to 3D drainage.

The centreline film thickness on the long wall, scaled by hydraulic radius R_h, is aspect-ratio-independent. Furthermore, it is about half the value for a circular tube. Inertia causes the side film to first thin then thicken with increasing Re.

The work also notes that even small Bond numbers ($Bo < 1$) can induce buoyancy-driven asymmetry in horizontal channels.

2.2 Interferometry

2.2.1 Introduction

Optical interferometry is a measurement technique that exploits the interference of light waves to extract information, particularly in applications like determining the thickness of thin films. There are two primary types of interferometry techniques: laser interferometry (LI) and white light interferometry (WLI), each with distinct advantages and limitations. In this study, we chose to work with WLI because of its higher accuracy and absolute measure.

Laser interferometry employs monochromatic light sources, resulting in interference patterns that are typically represented as gray-scale images. While highly coherent, this large coherence length can lead to unwanted interference from optical components in the experimental setup, making the technique less effective when dealing with complex or thick structures.

On the other hand, white light interferometry (WLI) offers a significant advantage due to the shorter coherence length of white light, which typically ranges on the order of micrometers (E. Hecht, Optics, 5th ed., Pearson, 2017, page 326). This leads to fewer spurious interference effects and produces colored interference patterns, making it better suited for precise measurement of layered structures, especially when thicker optical components are involved. WLI is widely adopted in industries like semiconductor manufacturing and materials science for high-precision metrology of thin films and surface profiling.

2.2.2 Scalar beam Interference

In Fig. 2.3, the rays R_1 and R_2 represent the interfering electromagnetic waves reflected from interfaces $PMMA/Water$ and $Water/Air$ respectively. The ray R_0 does not interfere with the others because the PMMA thickness H is much larger than the coherence length. Assuming that the incident light is not polarized and at normal incidence (so θ_i, θ_1, θ_2 are all zero at figure 2.3), so that there is no effect of polarization upon reflection, the electrical fields associated to them are given by

$$I = |E_1 + E_2|^2 + I_0, \tag{2.28}$$

where

$$E_1 = \sqrt{I_1}, \tag{2.29}$$

$$E_2 = \sqrt{I_2}\exp(i\Omega_{12}), \tag{2.30}$$

Ω_{12} is the term that accounts for the path and phase differences between R_1 and R_2, so that $\Omega_{12} = 2\pi\Delta_{12}/\lambda$, being Δ_{12} given by

$$\Delta_{12} = P_{12} + \phi_{12}\lambda = P_{12} + \frac{\varphi_1 - \varphi_2}{2\pi}\lambda, \tag{2.31}$$

Where:

- P_{12} is the optical path difference $2n_2h$
- φ_1, φ_2 are the phase shifts of rays R_1 and R_2 at reflection.

- ϕ_{12} is the net phase shift coefficient
- λ is the wavelength

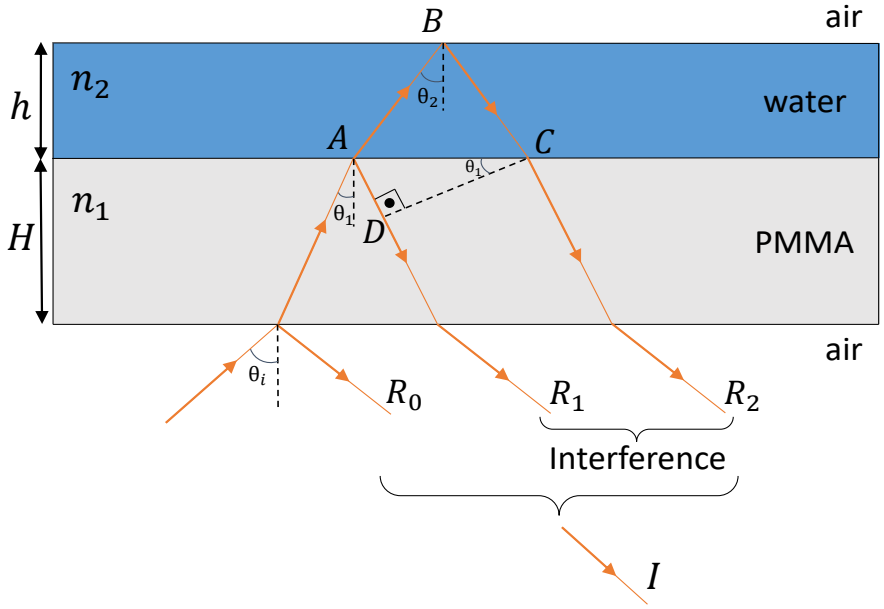

Figure 2.3: Single Layer Interference: Measure of h

After the above expressed equations, Eq. 2.28 can be rewritten as

$$I = I_0 + I_1 + I_2 + 2\sqrt{I_1 I_2}\cos\varphi_{12} \tag{2.32}$$

or still:

$$I = I_0 + I_1 + I_2 + 2\sqrt{I_1 I_2}\cos\frac{2\pi\Delta_{12}}{\lambda} \tag{2.33}$$

Only the last term of the sum has information about the layer thickness, and so that is the one to be used in this analysis.

2.2.3 Layer thickness determination

To determine the thickness of thin films using interferometry data, two prominent analytical methods are frequently applied:

Curve Fitting of Intensity vs. Wavelength (I(λ)): In this approach, the intensity of the reflected light is recorded across various wavelengths. By fitting theoretical models to the experimental intensity-wavelength curve, one can accurately

derive the thickness of the layer. This method is especially effective when dealing with uniform thin (less than 1μ) films. QUINTEN (2019)

Fast Fourier Transform (FFT) Method: The FFT method converts the interference data from the spectral domain into the frequency domain, allowing for the identification of periodic signals corresponding to the optical path difference.

Curve Fitting of Intensity vs. Wavelength (I vs. λ)

While the FFT method is powerful for determining the primary frequency of interference oscillations, it can be limited by the discrete nature of the Fourier transform and spectral leakage, particularly for very thin films or when high precision is required. An alternative and often more robust approach involves fitting the entire experimentally measured spectral intensity profile $I_{\text{exp}}(\lambda)$ to a theoretical interference model $I_{\text{theo}}(\lambda)$ using non-linear regression.

Theoretical Model. As derived in Eq.(2.33), the theoretical intensity for a given film thickness h and wavelength λ can be expressed generally as:

$$I_{\text{theo}}(\lambda, h) = I_0(\lambda) \left[1 + C(\lambda) \cos\left(\frac{4\pi n(\lambda) h}{\lambda} + \phi(\lambda)\right)\right], \tag{2.34}$$

where $I_0(\lambda)$ represents the background intensity, $C(\lambda)$ is the contrast (visibility) of the fringes, $n(\lambda)$ is the dispersive refractive index, and $\phi(\lambda)$ accounts for any phase shifts at the interfaces. In practice, the simplified model (assuming constant background and visibility locally) is often sufficient for fitting:

$$I_{\text{theo}}(\lambda, h) = A + B \cos\left(\frac{4\pi n(\lambda) h}{\lambda}\right), \tag{2.35}$$

where A and B are fitting parameters related to the mean intensity and fringe amplitude, respectively.

Objective Function. The goal is to find the thickness h that minimizes the difference between the experimental spectrum $I_{\text{exp}}(\lambda)$ and the theoretical model $I_{\text{theo}}(\lambda)$. This is formulated as a least-squares minimization problem. We define an objective function $\mathcal{F}(h)$ (often referred to as the residual sum of squares, RSS):

$$\mathcal{F}(h) = \sum_{i=1}^{N} \left[I_{\text{exp}}(\lambda_i) - K \cdot I_{\text{theo}}(\lambda_i, h)\right]^2, \tag{2.36}$$

where the summation runs over all N discrete wavelength points λ_i measured by the spectrometer. The factor K is a scaling parameter introduced to account for variations in absolute intensity levels between the measurement and the theoretical scale (e.g., due to exposure time or light source fluctuations).

Levenberg-Marquardt Algorithm. To solve this minimization problem, the Levenberg-Marquardt (LM) algorithm is typically employed. The LM algorithm is an iterative technique that interpolates between the Gauss-Newton algorithm (which is fast near the minimum) and the method of gradient descent (which is robust far from the minimum).

Starting from an initial guess h_0 (which can be effectively estimated using the FFT method described in Section 1.2.3), the algorithm iteratively updates the thickness parameter to reduce $\mathcal{F}(h)$ until convergence is reached. The fitting procedure determines the best-fit thickness h that explains the observed spectral fringes.

Sellmeier equation In the present approach, the film thickness is obtained by fitting the full measured spectrum with a theoretical model evaluated over the entire wavelength range. As a result, the variation of $n(\lambda)$ is inherently accounted for in the fitting procedure, and no additional dispersion correction is required, provided an appropriate model for $n(\lambda)$ is used.

The wavelength dependence of the refractive index is commonly described by the Sellmeier equation,

$$n^2(\lambda) = 1 + \sum_i \frac{B_i \, \lambda^2}{\lambda^2 - C_i}, \tag{2.37}$$

where B_i and C_i are material-specific coefficients.

Advantages of the Fitting Method. This approach offers significant advantages over simple peak-tracking (maxima/minima counting) methods:

1. **Noise Robustness:** By utilizing the entire spectral profile rather than just a few extremum points, the method averages out high-frequency random noise, acting as an effective filter.

2. **Sub-wavelength Precision:** Unlike peak counting, which is discrete (integer fringe orders), curve fitting is continuous, allowing for thickness resolution well

below the wavelength of light (often fractions of a nanometer).

Fast Fourier Transform (FFT) Thickness Determination

The determination of the liquid film thickness using the Fast Fourier Transform (FFT) relies on the periodic modulation of the measured optical spectrum caused by multiple-beam interference inside the film.

Interference signal and thickness information. From Eq. (1.34), the only term that carries information about the film thickness is the interference contribution

$$I_{\text{int}}(\lambda) = 2\sqrt{I_1 I_2}\,\cos\!\left(\frac{2\pi\Delta_{12}}{\lambda}\right),$$

where Δ_{12} is the optical path difference between the two interfering beams. For a single transparent layer of refractive index n_2 and physical thickness h, the dominant contribution to this phase delay is

$$\Delta_{12} \simeq 2n_2 h.$$

The interference term therefore takes the form

$$I_{\text{int}}(\lambda) \propto \cos\!\left(\frac{4\pi n_2 h}{\lambda}\right),$$

which shows that the measured spectrum exhibits oscillations whose periodicity is directly linked to the film thickness.

Change of variable to wavenumber. To make this periodicity explicit and suitable for Fourier analysis, the spectrum is rewritten as a function of the wavenumber

$$t = \frac{1}{\lambda}.$$

In this representation, the interference signal becomes

$$I_{\text{int}}(t) \propto \cos(4\pi n_2 h\, t)\,.$$

This expression is a simple cosine in the variable t, analogous to a harmonic signal in time. In this analogy:

- $t = 1/\lambda$ plays the role of an independent, time-like variable,
- the quantity $4\pi n_2 h$ acts as the physical angular frequency of the oscillation.

Interpolation onto an equidistant grid. A fundamental requirement of the FFT algorithm is that the input data must be sampled on an evenly spaced grid. In practice, spectrometers record intensity at discrete wavelengths, which generally leads to non-uniform spacing in the variable $t = 1/\lambda$.

Therefore, the measured spectrum must first be interpolated onto an equidistant grid in t, defined by

$$t_k = t_{\min} + k\,\Delta t, \qquad k = 0, \ldots, N-1,$$

with step size

$$\Delta t = \frac{t_{\max} - t_{\min}}{N} = \frac{1}{N}\left(\frac{1}{\lambda_{\min}} - \frac{1}{\lambda_{\max}}\right).$$

For computational efficiency, the number of samples N is typically chosen as a power of two, allowing the use of fast FFT algorithms.

Discrete Fourier transform and spectral peak. Once the spectrum is defined on an equidistant grid, the discrete Fourier transform is computed as

$$C_m = \sum_{k=0}^{N-1} I(t_k)\, e^{-i2\pi mk/N}.$$

The FFT tests a set of discrete angular frequencies

$$\omega_m = m\,\Delta\omega, \qquad \Delta\omega = \frac{2\pi}{N\,\Delta t},$$

and evaluates how strongly the measured signal correlates with each of them.

The power spectral density (PSD),

$$\mathrm{PSD}(m) = |C_m|^2,$$

exhibits a pronounced peak at an index m^* for which the trial frequency ω_{m^*} matches the physical oscillation frequency of the interference signal.

Thickness extraction. For a spectral window extending from $\lambda_{\min}$ to $\lambda_{\max}$, the FFT intrinsically defines a minimal resolvable thickness,

$$d_{\min} = \frac{1}{2n_2}\left(\frac{1}{\lambda_{\min}} - \frac{1}{\lambda_{\max}}\right),$$

which corresponds to the thickness producing one full interference oscillation over the measured wavelength range.

The film thickness is then obtained directly from the position of the dominant FFT peak as

$$h_{\mathrm{FFT}} = m^* \, d_{\min}.$$

Effect of refractive index dispersion. If the refractive index varies significantly over the spectral range, the use of a constant n_2 introduces a systematic error. A more accurate expression for the minimal thickness is obtained by accounting for dispersion at the spectral boundaries:

$$d_{\min} = \frac{1}{2} \left(\frac{n_2(\lambda_{\min})}{\lambda_{\min}} - \frac{n_2(\lambda_{\max})}{\lambda_{\max}} \right).$$

This correction substantially improves the accuracy of FFT-based thickness determination in dispersive materials.

Chapter 3

Methodology

3.1 Experimental Facility and Flow Loop

The experiment was conducted using a vertical flow loop designed to generate and study Taylor bubbles in a controlled adiabatic environment. The core of the test section consists of a rectangular millimetric channel with a cross-section of 2×5 mm and a length of 600 mm. The channel is oriented vertically to align with the direction of the flow and buoyancy forces.

The hydraulic circuit recirculates, with a pump, purified water at atmospheric pressure (1 bar). To prevent contaminants from affecting the sensitive optical measurements, the water is passed through a filtration system before entering the test section.

Taylor bubbles were generated at the base of the tube using a dedicated air injection system. Air was introduced via a capillary tube, with the injection rate precisely set by a mass flow controller. This configuration allowed for the generation of isolated Taylor bubbles with controlled lengths and velocities. The experiments covered a range of Bubble Capillary numbers (Ca_b) between 10^{-4} and 10^{-3}.

3.2 Optical Diagnostics and Instrumentation

To characterize the hydrodynamics and thin film dynamics of the Taylor bubbles simultaneously, the facility was instrumented with two synchronized optical diagnostic systems: high-speed shadowgraphy for macroscopic bubble dynamics and white

light interferometry for local liquid film thickness measurements.

3.2.1 High-Speed Shadowgraphy

The macroscopic behavior of the bubbles, including their shape, size, and rising velocity, was captured using a **Photron FASTCAM SA3** high-speed camera. The camera was positioned to view the 5 mm side of the channel.

- **Illumination:** The channel was back-lit using a high-intensity monochromatic diffuse LED, with a beam large enough for the whole section, to create a shadowgraph effect, rendering the interface of the gas bubbles as dark against a bright background.

- **Sensor Specifications:** The spatial resolution was determined experimentally using an optical calibration target composed of square features with known dimensions. The target was positioned at approximately the same distance from the imaging system as the bubble interface during the experiments, ensuring that the calibration was performed in the relevant object plane. Images of the target were acquired with the same optical configuration used in the measurements. Using the camera's image-processing software, the number of pixels corresponding to a known side length of the calibration squares was measured, yielding a spatial resolution of 8.5 μm/pixel. The use of telecentric lenses ensures a constant magnification across the field of view, so that this spatial resolution is uniform over the entire image.

3.2.2 White Light Interferometry (Spectrometry)

Local measurements of the thin liquid film thickness between the bubble and the tube wall were performed using an **Ocean FX Miniature Spectrometer**. This technique relies on the interference of broadband light reflected from the multiple interfaces of the liquid film (wall-liquid and liquid-gas).

- **Setup:** An optical probe connected to the spectrometer through an optical fiber was positioned at a specific height along the tube. Light from a white LED source was directed onto the channel wall. The reflected light, containing

the spectral interference pattern modulated by the film thickness, was collected by the probe and analyzed by the spectrometer.

- **Spectrometer Specifications:** The Ocean FX spectrometer was responsive in the 600–1000 nm spectral range. The integration time was of 1900μs so as to have a better quality of fringes and scan rates of 500 scans per second, which is critical for capturing the film thickness profile of a passing Taylor bubble.

3.3 Data Acquisition and Synchronization

A critical aspect of the methodology was the synchronization of macroscopic and microscopic measurements. Since the high-speed camera and the optical probe were located at different axial positions (separated by a distance Δd) along the tube, the data streams had to be temporally aligned.

A central waveform generator was used to trigger both the spectrometer and the high-speed camera simultaneously via TTL (Transistor-Transistor Logic) pulses. Both devices were set to operate at the same acquisition frequency. This common time-base allowed for the correlation of specific spectral measurements with the corresponding physical location on the bubble, accounting for the transit time required for the bubble to travel the distance Δd between the two sensors.

3.4 Data Processing and Analysis

The raw images acquired by the high-speed camera were processed using a custom automated algorithm developed in MATLAB to extract the bubble's geometric parameters and kinematics.

3.4.1 Image Segmentation and Feature Extraction

Prior to analysis, the raw grayscale images were converted to binary masks to isolate the gas phase from the liquid background. A static intensity threshold of $I_{th} = 29$ (on a 0–255 scale) was applied. This threshold was selected to robustly define the interface of the bubble against the back-lit illumination. It is important

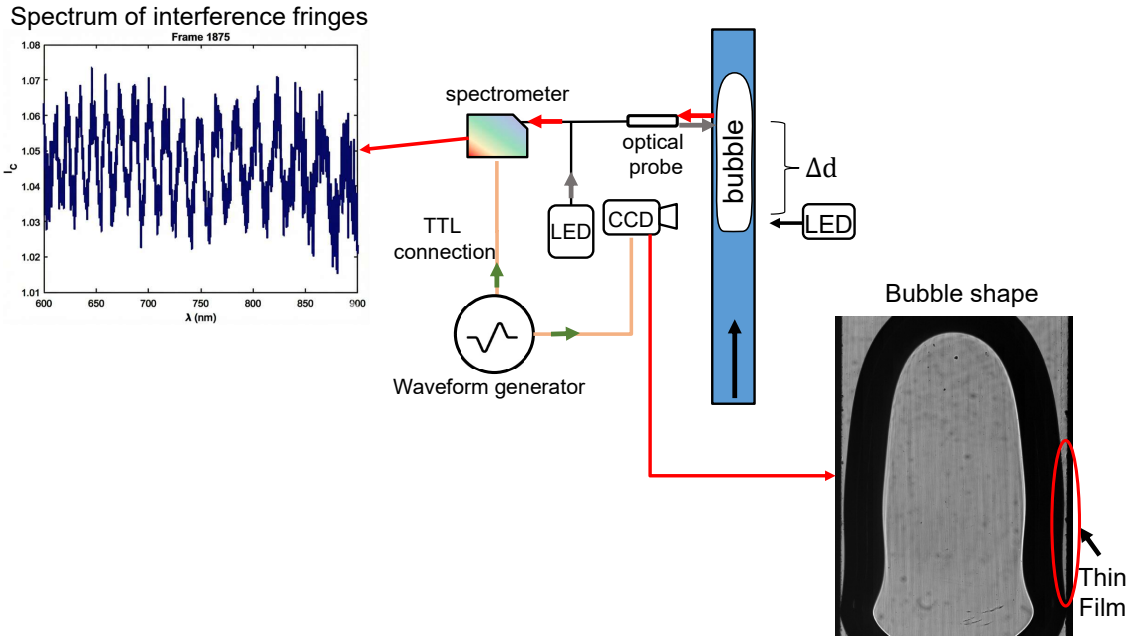

Figure 3.1: Schematic diagram of the complete experimental setup showing simultaneous data acquisition from the high-speed camera and spectrometer. The vertical rectangular channel (2 mm × 5 mm × 600 mm) is illuminated by a red LED source from behind for shadowgraphy imaging. The Photron FASTCAM SA3 [CCD] camera captures bubble kinematics at 500 fps, while the Ocean FX spectrometer measures film thickness via white-light interferometry using a fiber-optic probe positioned 85 mm downstream. Both instruments are triggered simultaneously by a shared TTL pulse from a waveform generator, ensuring temporal synchronization. Representative outputs are shown: a shadowgraphy image of the Taylor bubble (left) and a typical interference spectrum (right) used for film thickness extraction.

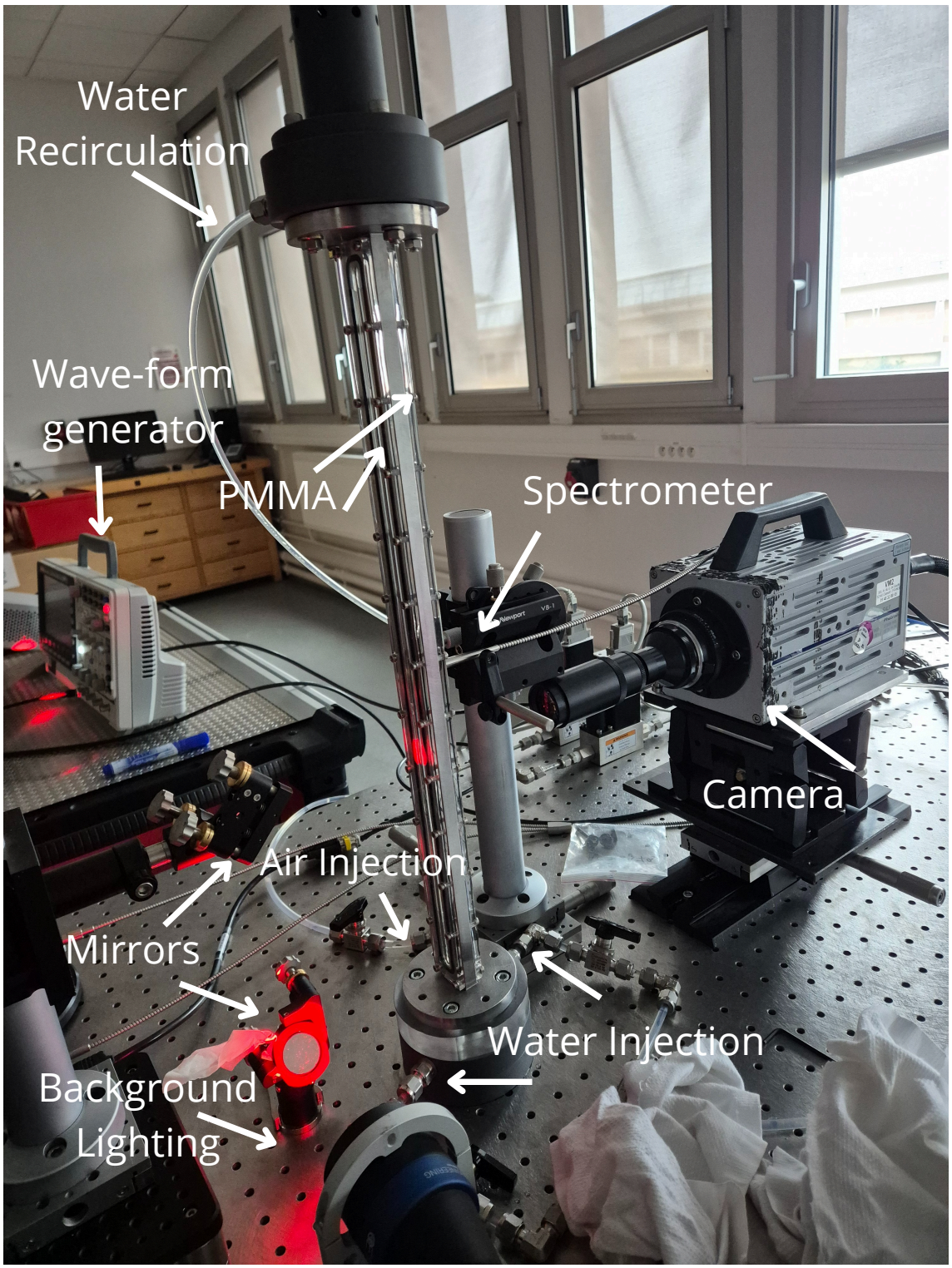

Figure 3.2: Photo of the experimental setup

to note that image intensity in the shadowgraph configuration does not directly correspond to the material phase. As seen in Fig. 3.3a, in the raw images, the liquid and flat gas phases appears bright due to uniform transmission of the back-light, whereas the gas–liquid curved interface appears dark as a result of strong refraction and light deflection. The solid channel walls also appear dark because they block or strongly attenuate the transmitted light. Consequently, in the binarized images, dark regions can correspond both to the gas phase and to the solid walls, while bright regions can correspond to the liquid and gas phases.

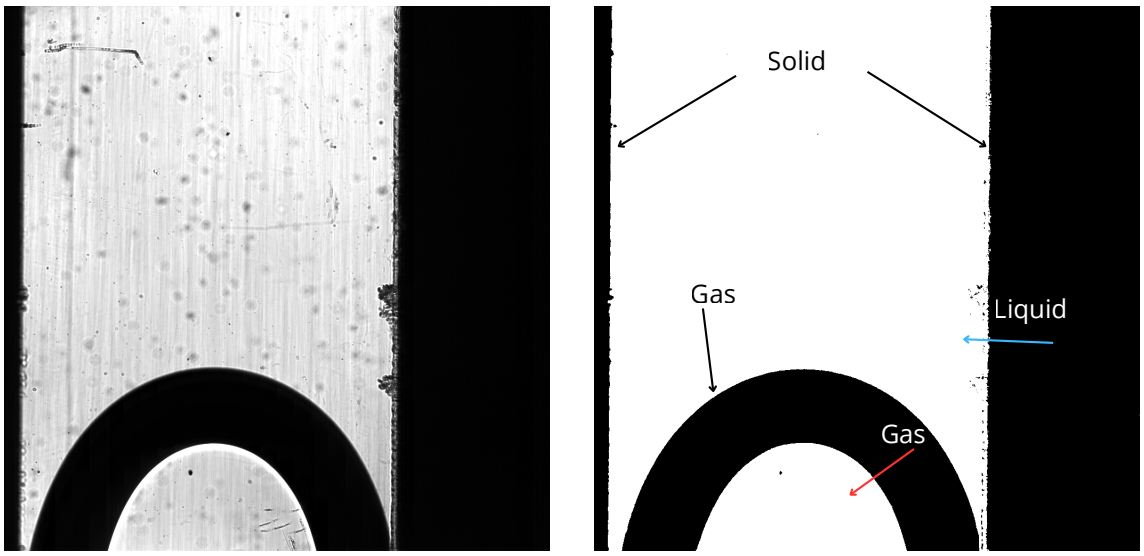

(a) Raw grayscale image

(b) Binarized image

Figure 3.3: Image binarization process for bubble edge detection. (a) Original 12-bit grayscale shadowgraphy image captured by the FASTCAM SA3. (b) Binary image obtained after applying a fixed threshold of 29, clearly distinguishing the gas bubble from the surrounding liquid phase.

3.4.2 Bubble Velocity Calculation

The bubble rise velocity (U_b) was determined by tracking the displacement of the bubble's leading meniscus across consecutive frames.

1. **Edge Detection:** The algorithm scans a fixed horizontal row (or vertical column depending on orientation) to identify the specific pixel coordinates (x, y) corresponding to the gas-liquid interface transition (from 0 to 1 in the binary mask).

2. **Displacement Tracking:** The Euclidean distance in pixels (d_{px}) between the interface coordinates in frame i and frame $i + \Delta t$ was calculated.

3. **Velocity Computation:** The velocity was computed using the spatial resolution ($C_{cal} = 8.5$ μm/px) and the temporal resolution of the camera (500 fps, corresponding to $\Delta t = 2$ ms). The resulting speed is given by:

$$U_b = \frac{d_{px} \cdot C_{cal}}{\Delta t} \tag{3.1}$$

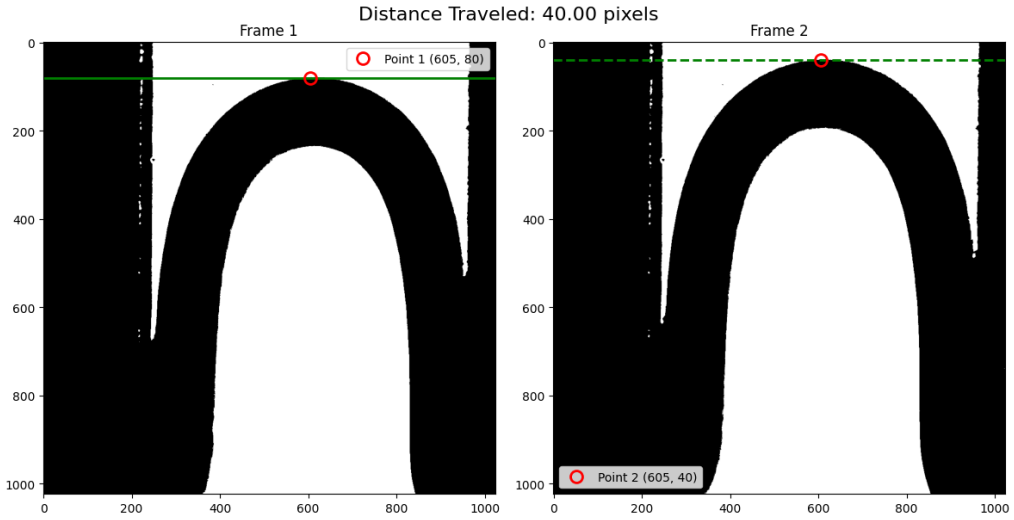

Figure 3.4: Bubble speed calculation using a fixed-point tracking method. Two consecutive frames captured at 500 fps ($\Delta t = 2$ ms) show the bubble nose displacement. A fixed horizontal line (green dashed line) at $y = 80$ pixels in Frame 1 identifies Point 1 at coordinates $(605, 80)$. The same x-coordinate ($x = 605$) is tracked in Frame 2, where the interface has moved to Point 2 at coordinates $(605, 40)$. The vertical displacement of 40 pixels corresponds to a physical distance of 340 μm (using the 8.5 μm/px calibration), yielding a bubble speed of 0.17 m/s.

3.4.3 Bubble Size Estimation

The bubble length (size) was calculated by combining the bubble's translational movement with the geometric length measured in the images. Since the bubble is often larger than a single field of view or moves significantly between frames, the algorithm accounts for the number of frames elapsed (N_{frames}) between the capture of the bubble nose and the bubble tail. The total length is derived from the vertical

pixel distance measured in the frame plus the distance the bubble traveled during the frame interval.

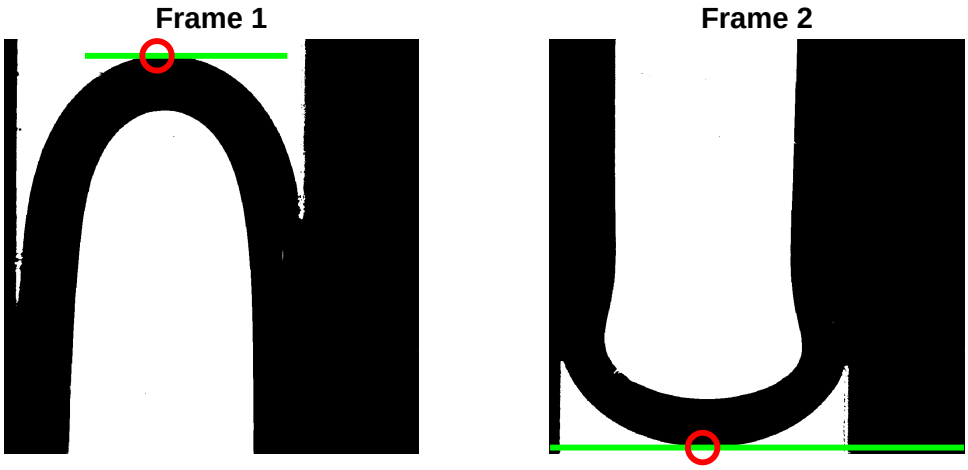

Figure 3.5: Bubble size (length) calculation methodology. The bubble length is determined by tracking the nose position across frames. Using the known bubble speed U_b from the velocity measurement and the time interval between frames (determined by frame numbers and frame rate), the streamwise distance traveled by the bubble is calculated. The size is computed as $L_b = \Delta y_{\text{frames}} + \Delta x_{\text{travel}}$, where Δy_{frames} is the vertical pixel distance between the nose and tail positions in Frame 1 and Frame 2, and $\Delta x_{\text{travel}} = U_b \cdot \Delta t_{\text{frames}}$ accounts for the bubble displacement during the acquisition interval. The physical length is obtained using the 8.5 μm/px spatial calibration factor.

3.4.4 Curvature and Radius of Curvature

Unfortunately, a direct comparison with the predicted meniscus curvature is not possible in the present configuration. The curvature that governs film deposition is the streamwise curvature of the rear meniscus in the same plane as the deposited film. In contrast, the bubble shape is measured in the plane of the 5 mm channel, while the film thickness is measured in a different location. As a result, the experimentally accessible curvature does not correspond to the curvature component responsible for film deposition, preventing a quantitative comparison with theoretical predictions. To characterize the nose shape, the radius of curvature in the 5 mm plane (R_c) was determined using an algebraic circle-fitting approach known as **Taubin's Method**.

1. **Boundary Extraction:** The `bwboundaries` function was used to extract the coordinates of the bubble perimeter from the binary image.

2. **Filtering:** The contour data was filtered to remove artifacts and select only the relevant points belonging to the nose meniscus.

3. **Taubin's Fit:** The algorithm solves a linear system of moments derived from the contour points (x, y) to minimize the algebraic distance to a circle. This method is preferred for its stability and non-iterative nature compared to standard geometric fits. It outputs the center coordinates (x_c, y_c) and the radius R directly.

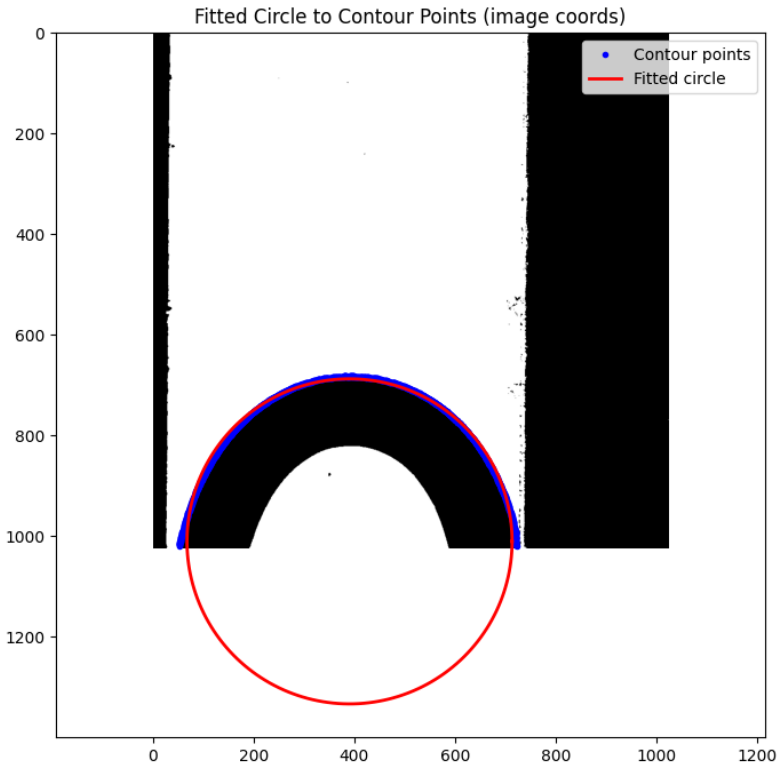

Figure 3.6: Fitted circle to contour points in image coordinates.

3.5 Interferometry Characterization and Validation

Before conducting the Taylor bubble experiments, the interferometric technique underwent a characterization phase to assess the feasibility of fringe detection, op-

timize the signal-to-noise ratio (SNR), and validate the accuracy of the thickness measurements.

3.5.1 Feasibility Study: Fringe Observation

The first stage of the process involved establishing whether interference fringes could be successfully observed given the specific optical properties of the test section. The challenge lies in the relatively low refractive index contrast between the PMMA channel wall ($n \approx 1.49$) and water ($n \approx 1.33$), which results in weak reflection coefficients compared to glass-air interfaces.

To verify the observability of fringes, a preliminary test - represented at Figure 3.7 was conducted using ethanol. Ethanol was selected because its refractive index ($n \approx 1.36$) is comparable to that of water, making it a suitable optical analogue for the Taylor bubble experiments. A thin layer of ethanol was deposited on the inner wall of the tube. Due to the high volatility of ethanol, the liquid film evaporated rapidly, naturally thinning over time. This dynamic evaporation process allowed the film to sweep through a wide range of thicknesses, including extremely thin layers that would be difficult to generate and stabilize using mechanical means.

The observation of distinct interference fringes during the ethanol evaporation confirmed that the optical setup was sensitive enough to resolve the constructive and destructive interference patterns required for thickness calculation, despite the low reflectivity of the wall-liquid interface.

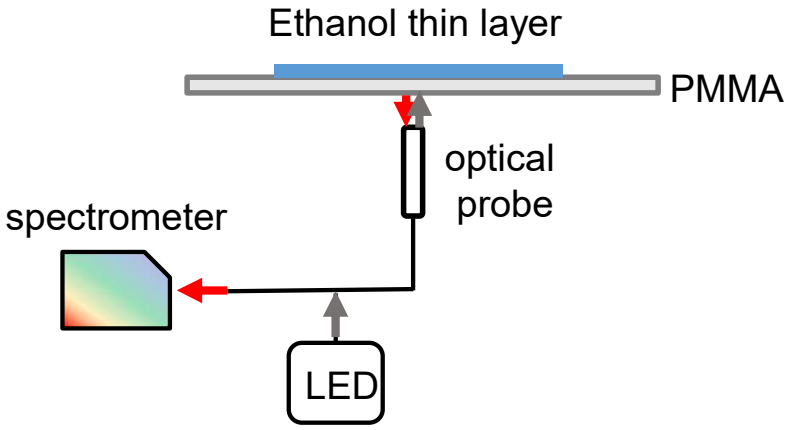

Figure 3.7: Schematics of the test with ethanol to verify the observability of fringes

To further verify the detection capability, a direct comparison was made between

the baseline spectral signature and the signal obtained during the presence of a liquid film. Figure 3.8 presents the reference spectrum reflected from the dry channel wall (representing the white light source characteristics) alongside a spectrum acquired with a thin ethanol layer present. While the overall intensity profile follows the source spectrum, distinct interference modulations (fringes) are clearly superimposed on the signal when the film is present. This confirms that the optical setup has sufficient sensitivity to resolve phase differences caused by thin liquid layers, despite the low refractive index contrast.

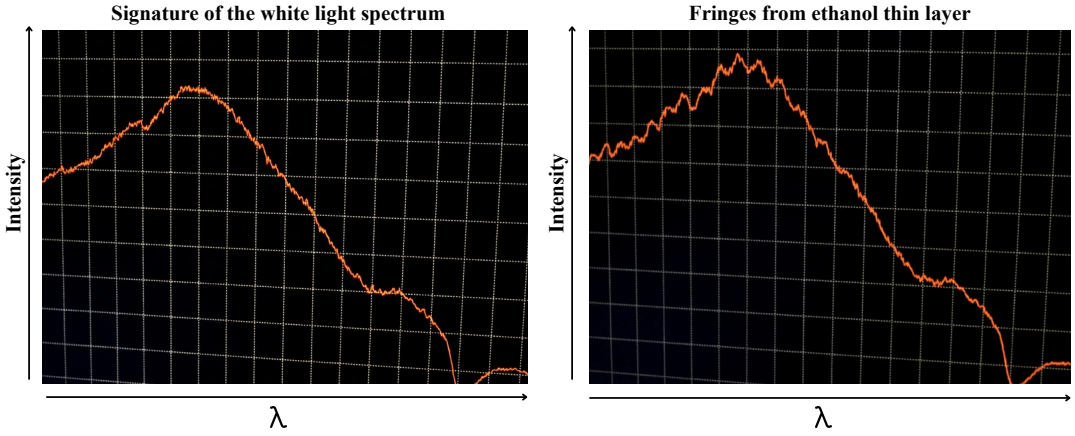

Figure 3.8: Spectral comparison demonstrating the fringes from the thin ethanol layer

To visualize this compromise, Figure 3.10 presents typical spectral data obtained under different integration time settings. One case demonstrates a high-SNR acquisition characterized by clear, smooth fringes suitable for accurate analysis, but obtained at a lower temporal resolution due to the required long integration time. Conversely, a second case shows data acquired at a higher frequency (shorter integration time), revealing a significant increase in noise levels. This noise can obscure the interference pattern, hindering accurate thickness retrieval. This comparison highlights the necessity of selecting operating parameters that prioritize fringe clarity over maximum acquisition speed for this specific application.

3.5.2 Signal-to-Noise Ratio (SNR) Optimization

To ensure the reliability of the interferometric measurements, the quality of the spectral fringes was quantified using the Signal-to-Noise Ratio (SNR).

The SNR was determined by analyzing the contrast between the interference fringes and the background signal noise. Specifically, the fringe amplitude A was derived by identifying the local maxima and minima of the spectral signal. The noise level was characterized by the standard deviation σ of the signal. The SNR was then calculated in decibels (dB) using the following expression:

$$SNR = 10 \log_{10} \left(\frac{A}{\sigma} \right) \tag{3.2}$$

Figure 3.9 illustrates this process, identifying the extrema used to compute the amplitude relative to the noise.

Spectral Pre-processing: Background Subtraction and Normalisation The raw spectral signals (I_v) were processed to obtain a compensated intensity value (I_c) that is normalised and free from ambient background noise. The three-step procedure is defined by the equation:

$$I_c = \frac{I_v - I_d}{I_r - I_d} \tag{3.3}$$

The constituent spectra were obtained under the following specific operational states:

(a) Dark Spectrum (I_d): Acquired with the light source deactivated (water flowing, no air injection). This spectrum captures the constant background signal from the ambient environment, which is subsequently subtracted from all measurements to remove this systematic offset.

(b) Reference Spectrum (I_r): Acquired with the light source activated under a baseline condition (water flowing, no air injection). This provides a reference signal against which all active measurements are normalised.

(c) Variable Spectrum (I_v): The raw spectrum of interest, acquired with the light source activated and both water and air injection flowing.

Following this quantification, the acquisition parameters were optimized. A critical trade-off was identified between the acquisition frame rate and the SNR. The SNR is governed largely by the integration time of the spectrometer; longer integration times collect more photons, resulting in clearer, more defined fringes (higher SNR), but inherently limit the maximum acquisition frequency.

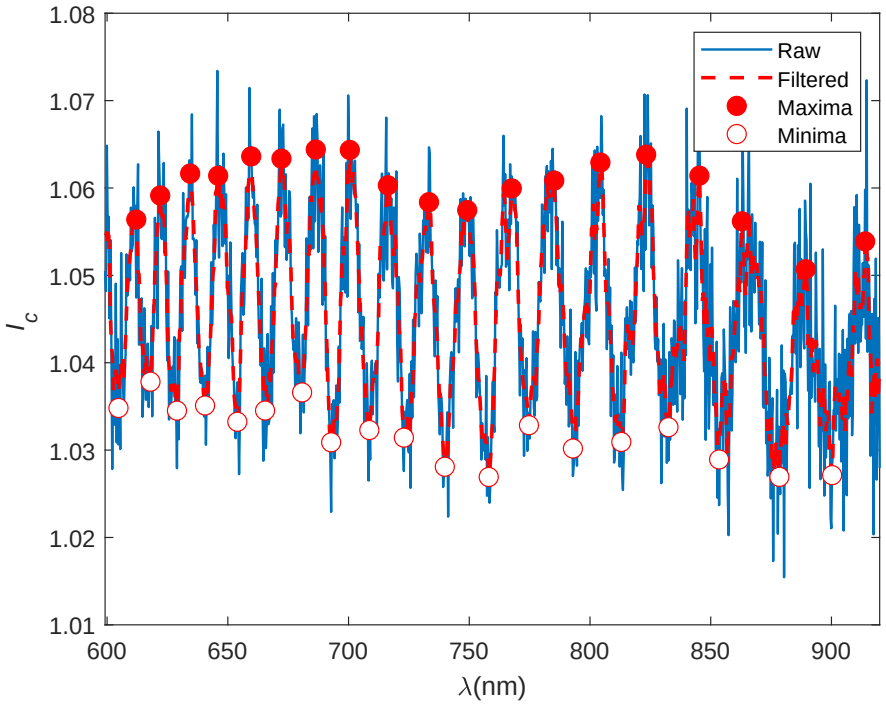

Figure 3.9: Spectral-resolved interference. The raw spectral signal is processed to identify local maxima (red) and minima (green). These extrema allow for the determination of the fringe amplitude A, which is related to the signal standard deviation σ to quantify the SNR.

To visualize this compromise, Figure 3.10 presents typical spectral data obtained under different integration time settings. One case demonstrates a high-SNR acquisition characterized by clear fringes suitable for accurate analysis but obtained at a lower temporal resolution. Conversely, a second case shows data acquired at a higher frequency (shorter integration time), revealing a significant increase in noise levels that can obscure the interference pattern.

Given the priority to accurately resolve the film thickness, the decision was made to prioritize SNR over temporal resolution. The integration time was adjusted to achieve a "reasonable" SNR that guaranteed identifiable fringes, accepting a reduction in the number of thickness data points available per bubble transit.

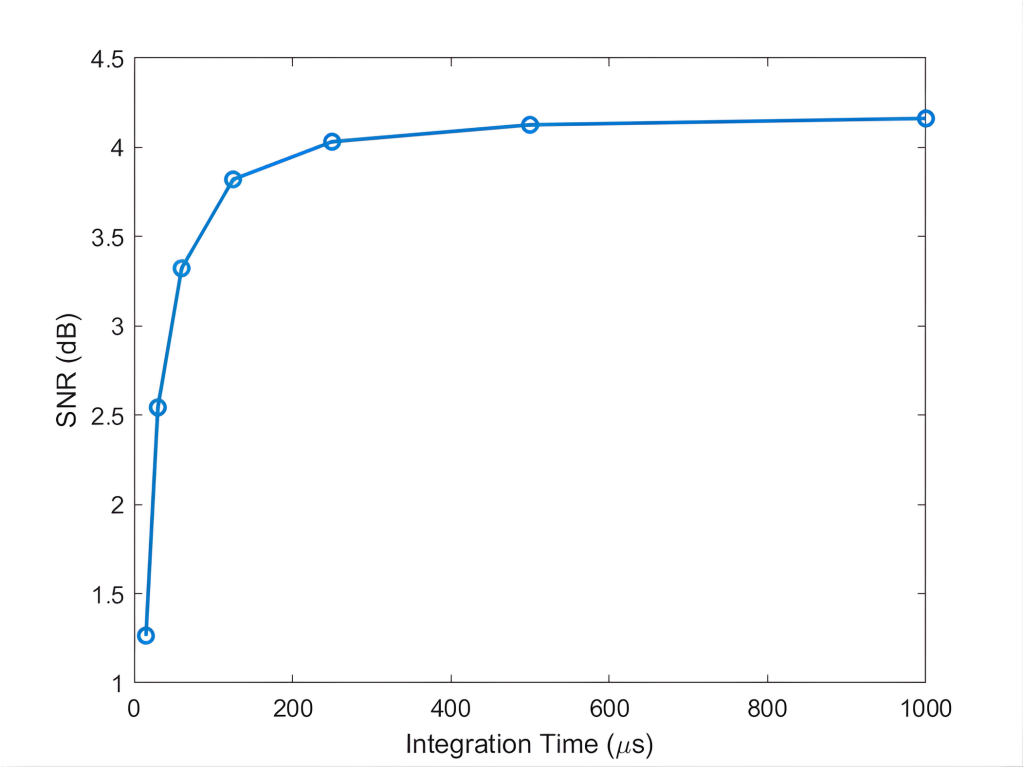

Figure 3.10: Illustration of the trade-off between SNR and acquisition frequency. Reducing integration time to increase the frame rate degrades the SNR, making interference fringes difficult to distinguish from noise. A compromise was selected to ensure fringes were resolvable while maintaining adequate temporal resolution.

3.5.3 System Validation

To validate the accuracy of the measurement encompassing the optical probe, spectrometer, and the custom post-processing algorithm, a calibration test was per-

formed using a standard reference target. An Indium Tin Oxide (ITO) coated glass sample was selected as the reference standard due to its stable optical properties and known manufacturing specifications.

The manufacturer specified the ITO coating thickness to lie within the interval of $950 - 1000$ nm. The optical probe was directed at the ITO sample, and the resulting interference spectra were acquired using the same parameters optimized for the experimental campaign. These raw spectra were then processed using the in-house code developed for this study.

The algorithm calculated a film thickness of 968 nm. This result falls squarely within the manufacturer's specified tolerance range ($950 - 1000$ nm), confirming the system's capability to correctly interpret spectral data and output accurate physical thickness values. This successful validation provided the necessary confidence to apply the technique to the dynamic liquid films of Taylor bubbles.

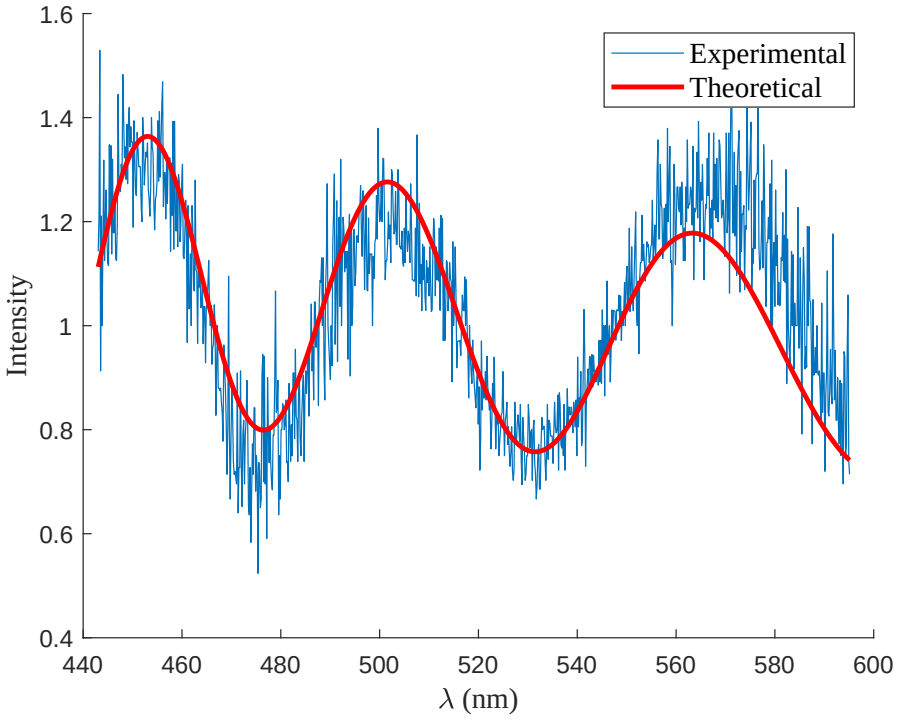

Figure 3.11: Validation of the interferometric technique using an ITO coated glass reference. The in-house code derived a thickness of 968 nm from the experimental spectra, which agrees with the manufacturer's specified range of 950–1000 nm, validating the measurement accuracy.

Chapter 4

Results

4.1 Experimental Campaign and Results

A series of ten experimental tests were conducted to characterize the dynamics of Taylor bubbles within the rectangular channel (2×5 mm cross-section). The experiments operated under adiabatic conditions using air and water as the working fluids at atmospheric pressure (1 bar). The primary control parameters were the injection rates for the gas and liquid phases, which were varied to span a specific range of Capillary numbers (Ca_{bubble}), effectively covering the regime $10^{-4} \leq Ca_{bubble} \leq 10^{-3}$. Also, the range of Reynolds number was $8.10^1 \leq Re_{bubble} \leq 6.10^2$ and Bond number Bo was 0.13

The quantitative results of the experimental campaign are summarized in Table 4.1. As the gas or water injection rate increased, a corresponding increase in bubble velocity was observed, ranging from approximately 0.029 m/s to 0.22 m/s. For the columns of the table, there is the following equivalence: Air injection = Q_a / Water injection = Q_w / Bubble Speed = U_b / Measured thickness = h / Curvature Radius R_c

4.2 Liquid Film Dynamics and Comparison with Correlations

The experimental measurements of the dimensionless film thickness (h/r) were plotted against the Capillary number (Ca) to evaluate the agreement with estab-

Table 4.1: Summary of experimental conditions and measured parameters.

Q_a **(ml/min)**	Q_w **(ml/min)**	Ca_{bubble}	U_b **(m/s)**	h **(μm)**	R_c **(mm)**	Re_{bubble}
50	70	3.05×10^{-3}	0.22	22.2	2.0	627
50	60	2.72×10^{-3}	0.19	21.1	2.0	542
40	35	2.06×10^{-3}	0.15	15.0	2.1	428
30	20	1.65×10^{-3}	0.11	14.3	2.1	341
30	5	1.35×10^{-3}	0.10	12.4	2.1	279
27	5	9.90×10^{-4}	0.07	11.3	2.1	205
20	5	8.45×10^{-4}	0.06	10.0	2.1	175
15	5	7.46×10^{-4}	0.05	9.2	2.1	155
10	5	5.47×10^{-4}	0.04	7.7	2.1	113
5	5	3.96×10^{-4}	0.03	5.8	2.2	82

lished theoretical models.

Figure 4.1 presents a comparison between the measured dimensionless film thickness h/r and established correlations as a function of bubble capillary number Ca_b. The experimental data show a clear monotonic increase of h/r with Ca_b, which is qualitatively consistent with all three reference models.

In this analysis, r is defined as half the length of the channel side lying in the same plane as the measured film thickness. This choice follows from the understanding that, for a Taylor bubble in a rectangular channel, the local film thickness at a given plane is primarily governed by the bubble's curvature in that plane. Since the bubble curvature cannot be measured directly, it is common practice to approximate the relevant length scale as half the local channel dimension in the plane of interest. This approach is supported by studies of Taylor bubbles in non-circular conduits, where the film thickness near a wall scales with the local radius of curvature of the bubble, which in turn is approximated by half the channel dimension in that direction MAGNINI *et al.* (2022). Consequently, for our $2 \times 5\,\text{mm}$ channel, the

relevant dimension in the plane of measurement is 1 mm.

The correlation proposed by HAN e SHIKAZONO (2009), shown by the red dashed line, systematically predicts larger film thicknesses than those measured in the present experiments. This overestimation is consistent with their experimental conditions, which involved circular microtubes and extended to relatively high Reynolds numbers, where inertial effects significantly enhance liquid film deposition.

$$\frac{h}{D} = \begin{cases} \dfrac{0.670\,Ca^{2/3}}{1 + 3.13\,Ca^{2/3} + 0.504\,Ca^{0.672}Re^{0.589} - 0.352\,We^{0.629}}, & Re < 2000, \\ \dfrac{106.0\left(\dfrac{\mu^2}{\rho\sigma D}\right)^{2/3}}{1 + 497.0\left(\dfrac{\mu^2}{\rho\sigma D}\right)^{2/3} + 7330\left(\dfrac{\mu^2}{\rho\sigma D}\right)^{0.672} - 5000\left(\dfrac{\mu^2}{\rho\sigma D}\right)^{0.629}}, & Re > 2000. \end{cases} \tag{4.1}$$

In the present experiments, the Reynolds number always satisfies $Re < 2000$, and therefore only the first expression is relevant for comparison with the measured film thickness.

The model of AUSSILLOUS e QUÉRÉ (2000), represented by the green dash-dotted curve, provides intermediate predictions. Although it captures the overall scaling with Ca_b, it still slightly overpredicts the experimental values, what was expected since it was derived for circular tubes. The larger film thickness predicted suggests that inertial corrections embedded in this formulation remain partially active even at the relatively low capillary numbers explored here.

$$\frac{h}{D} = \frac{0.67\,Ca^{2/3}}{1 + 2.5 \times 1.34\,Ca^{2/3}} \tag{4.2}$$

In contrast, the correlation by MAGNINI *et al.* (2022), shown by the blue dotted line, is in closest agreement with the experimental measurements over the entire investigated range of Ca_b. This improved agreement highlights the importance of geometric effects, since the formula was derived for rectangular capillaries, and three-dimensional drainage mechanisms, which tend to reduce the effective film thickness compared to classical circular-tube correlations.

$$\frac{h}{R_h} = \frac{0.7\,Ca^{2/3}}{1 + 3.35\,Ca^{2/3}} \tag{4.3}$$

Overall, this comparison indicates that the present experiments are conducted in a predominantly visco-capillary regime with limited inertial influence, and that

models accounting for confinement-induced drainage provide a more accurate description of the observed film thickness.

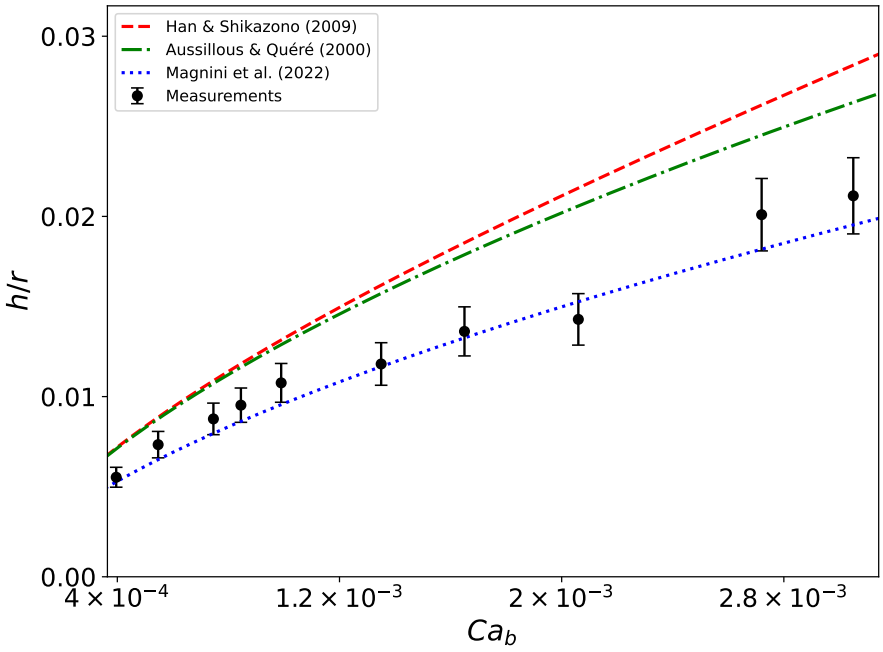

Figure 4.1: Comparison of measured dimensionless film thickness (h/r) against Capillary number (Ca_b) and established correlations.

4.3 Numerical simulations using OpenFOAM

Complementary to the experimental investigation, three-dimensional numerical simulations of Taylor bubbles were performed by Mirco Magnini using the open-source CFD framework OpenFOAM (v2106). The simulations employed the `interFoam` solver, which is based on an algebraic Volume-of-Fluid (VOF) method for incompressible, immiscible two-phase flows.

The solver resolves the one-fluid formulation of the incompressible Navier–Stokes equations coupled with a transport equation for the liquid volume fraction. Surface tension effects are modeled using the Continuum Surface Force approach BRACKBILL *et al.* (1992). The numerical model therefore computes the transient evolution of the velocity field, pressure, and gas–liquid interface shape.

The simulated configuration corresponds to an air–water system in a vertical rectangular channel of height $H = 2$ mm and width $W = 5$ mm, yielding an aspect

ratio $AR = 2.5$. The characteristic length scale is the hydraulic radius,

$$R_h = \frac{2HW}{H+W} = 1.43 \text{ mm}.$$

In the nondimensional formulation adopted in the simulations, $R_h = 1$, $U_l = 1$, and $\rho_l = 1$, while the remaining physical properties were adjusted to match the prescribed liquid capillary number Ca_l, liquid Reynolds number Re_l, and Bond number Bo.

The simulations were performed in a reference frame translating upward at the imposed liquid velocity U_l. No-slip boundary conditions were applied at the channel walls with a velocity $-U_l$, while fully developed velocity conditions were imposed at the inlet and outlet. The initial bubble consisted of an elongated gas body with rounded caps and an initial length $L_{b,0} = 4.5\,w$, where $w = W/2$.

The computational mesh was three-dimensional and structured, with base resolutions $\Delta z = \Delta y = 0.0166\,R_h$ and $\Delta x = 0.0332\,R_h$. A near-wall refinement was applied down to a minimum cell size of $0.0005\,R_h$, using a growth rate of 1.3. This resolution allows liquid films as thin as approximately $0.003\,R_h$ to be accurately resolved. Time integration was performed using an adaptive time step constrained by a Courant number $Co = 0.1$, leading to time steps of order 10^{-4} and up to two orders of magnitude larger than the capillary time-step restriction in the most refined cells.

A first set of simulations was conducted at $Ca_l = 0.002$ and $Re_l = 418$, considering two gravitational conditions: $Bo = 0$ and $Bo = 0.275$. The simulations were advanced until a steady state was reached, after which the bubble shape and liquid film distribution were analyzed.

Figure 4.2a shows the streamwise evolution of the normalized film thickness δ_y/h along the bubble axis, plotted as a function of the dimensionless coordinate x/R_h. Here, $x/R_h = 0$ corresponds to the bubble front (nose), while negative values extend downstream along the bubble body toward the rear meniscus. The variable δ_y denotes the distance between the channel wall and the gas–liquid interface measured along the y-direction, normalized by the half-height of the channel $h = H/2$, the choice of symbols differs from the ones adopted on this thesis. However, δ_y/h is equivalent to h/r in 4.1

For both Bond numbers, a rapid decrease in δ_y/h is observed downstream of the

bubble front, followed by a nearly constant plateau of 13.4 mm corresponding to the fully developed deposited film. For $Bo = 0.275$, the film thickness was 16.4 mm making it systematically larger than in the gravity-free case, reflecting the influence of gravity and inertia on liquid redistribution around the bubble perimeter. These trends are consistent with experimental observations - the corresponding point is 15 mm in Table 4.1 - and with previous numerical studies MAGNINI *et al.* (2022).

4.4 Uncertainty Analysis and Experimental Considerations

The reliability of the measured film thickness (h) is evaluated through a dual-lens approach: characterizing the instrumental limits of the hardware (systematic) and the statistical behavior of the fitting algorithm under dynamic flow conditions (random).

4.4.1 Systematic Uncertainty: The Instrumental Floor

The systematic uncertainty defines the absolute precision limit of the experimental apparatus, regardless of the signal quality. The primary considerations for these limits are:

1. **Wavelength Calibration (σ_λ):** The Ocean FX spectrometer maps light onto a 2048-pixel CCD. With a dispersion of 0.195 nm/pixel [600-1000nm band], any spectral feature is subject to a discretization error. A conservative uncertainty of ± 0.2 nm (approx. 1 pixel) is adopted to account for factory calibration tolerances and potential slight shifts in the pixel-to-wavelength mapping.

2. **Refractive Index Stability (σ_n):** While the Sellmeier equation provides high-accuracy dispersion modeling, n is sensitive to environmental variables. An uncertainty of ± 0.002 is utilized to encompass:

    - Thermal fluctuations in the liquid phase (± 2°C).
    - Minor impurities or concentration gradients in the working fluid.

- Inherent tolerances in the Sellmeier coefficients for water and PMMA.

The combined systematic relative uncertainty is calculated using the root-sum-square method, assuming independent variables:

$$\frac{\sigma_{sys}}{h} = \sqrt{\left(\frac{\sigma_n}{n}\right)^2 + \left(\frac{\sigma_\lambda}{\lambda}\right)^2} = \sqrt{\left(\frac{0.002}{1.33}\right)^2 + \left(\frac{0.2}{800}\right)^2} \approx 0.152\% \tag{4.4}$$

This result confirms that the hardware provides an exceptionally stable "ruler," with a systematic error floor of only ± 35 nm at the maximum measured thickness of 23 μm.

4.4.2 Random and Fitting Uncertainty: Signal Robustness

Unlike systematic errors, the fitting uncertainty (σ_{fit}) is dynamic and depends on the quality of the interference fringes captured during the experiment.

1. **The Fitting Process:** The in-house algorithm minimizes a cost function comparing the measured spectrum to a theoretical model. The uncertainty σ_{fit} is extracted from the diagonal elements of the covariance matrix.

2. **The PMMA-Water Interface Challenge:** A significant consideration in this study is the low refractive index contrast (1.49 vs. 1.33). This results in low-amplitude fringes and a low Signal-to-Noise Ratio (SNR), making σ_{fit} the dominant term in the total uncertainty budget.

With the information presented above, it is observed that the biggest part of the uncertainty comes from the fitting error of the theoretical curve and the experimental one due to low SNR.

4.4.3 Hydrodynamic Influence of the Bubble Train

The measurements were performed within a **bubble train (slug flow)** regime, which introduces physical phenomena absent in isolated Taylor bubble studies:

- **Wake Interaction and Inertial Ripples:** In a bubble train, the wake of the leading bubble modifies the pressure field for the succeeding one. As the Capillary number (Ca) increases, inertia triggers undulations and "ripples" on the liquid-gas interface.

- **Impact on Data:** These ripples cause the local film thickness to fluctuate rapidly. While the spectrometer integration time is optimized, these physical undulations manifest as an increased standard deviation in the thickness data. Thus, the observed uncertainty at higher Ca is not merely a measurement error, but a reflection of the inherent interfacial instability of the bubble train.

In summary, the 200 μm fiber and the full-spectrum fitting method successfully resolve thicknesses up to 23 μm, maintaining a high degree of confidence despite the hydrodynamic complexities of the slug flow regime.

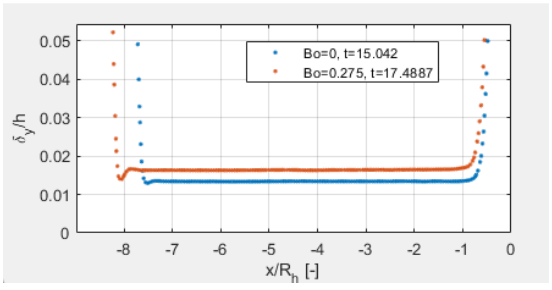

(a) Film thickness profile along the bubble axis for $Bo = 0$ and $Bo = 0.275$.

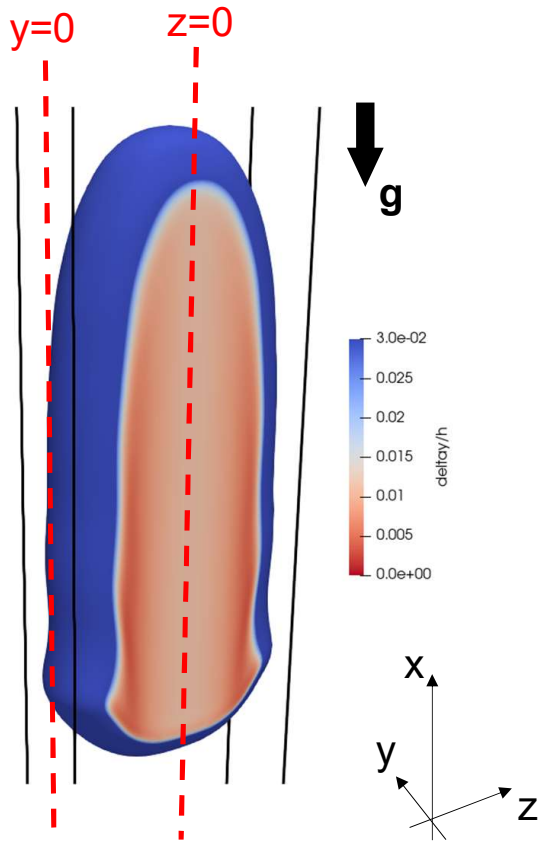

(b) 3D view of the Taylor bubble showing the spatial distribution of δ_y/h.

Figure 4.2: Numerical OpenFOAM results for the liquid film around the Taylor bubble.

Chapter 5

Conclusion

This study successfully characterized the experimental facility and methodology required to investigate the dynamics of Taylor bubbles and the associated liquid film thickness in rectangular micro-channels. High-resolution and high-speed optical techniques were employed, specifically validating white light interferometry as a precise tool for film thickness measurement despite the challenges posed by low signal-to-noise ratios.

The primary conclusions drawn from this work are:

1. **Optical Technique Validation:** While the similar refractive indices of PMMA and water created a low SNR environment, the development of an in-house processing code based on theoretical fitting allowed for the successful extraction of film thickness data, overcoming the limitations of standard commercial software.

2. **Experimental Trends:** The experimental data covers a range of Capillary numbers from 10^{-4} to 10^{-3}. The measured film thickness shows a strong correlation with the Capillary number, and the results align most closely with the theoretical predictions of Magnini et al. (2022).

3. **Numerical Insights:** OpenFOAM simulations highlighted the importance of inertial and gravitational effects (Bond number), revealing characteristic undulations in the liquid film that suggest a complex, three-dimensional flow structure near the wall. In addition, the increased thickness found experimentally for most points in comparison to Magnini's curve can possibly be

explained by the non inclusion of Bond number on his curve.

4. **Rectangular versus Circular tubes**: In similar conditions, the rectangular tubes seem to have a thinner layer than in circular ones, possibly because of capillary pressure gradients induced by geometric curvature differences, which generate a capillary suction force driving liquid toward the corners.

5.1 Ongoing Work and Next Steps

Current efforts are focused on the continued post-processing of the experimental data to refine the correlations between film thickness, speed, size, and meniscus curvature across a broader range of Capillary numbers. Future steps will involve extending the comparison between the experimental findings and the 3D numerical simulations to fully elucidate the physics of near-wall phenomena, specifically the triggering of wall drying and the motion of the contact line.

Bibliography

KHODAPARAST, S., MAGNINI, M., BORHANI, N., et al. "Dynamics of isolated confined air bubbles in liquid flows through circular microchannels: an experimental and numerical study", *Microfluid Nanofluid 19, 209–234 (2015)*, 2015.

BORHANI, N., AGOSTINI, B., THOME, J. R. "A novel time strip flow visualisation technique for investigation of intermittent dewetting and dryout in elongated bubble flow in a microchannel evaporator", *International Journal of Heat and Mass Transfer*, v. 53, n. 21, pp. 4809–4818, 2010. ISSN: 0017-9310. doi: https://doi.org/10.1016/j.ijheatmasstransfer.2010.06.011. Disponível em: <`https://www.sciencedirect.com/science/article/pii/S0017931010003157`>.

WHALLEY, P. B., AZZOPARDI, B. J., HEWITT, G., et al. "A Physical Model for Two Phase Flows with Thermodynamic and Hydrodynamic Non-Equilibrium". In: *Proceedings of the 7th International Heat Transfer Conference*, pp. 181–188, Department of Engineering Science, University of Oxford, U.K., 1982. doi: 10.1615/IHTC7.570.

WHALLEY, P. B. *Boiling, Condensation, and Gas-Liquid Flow.* Oxford Oxfordshire; New York, Clarendon Press; Oxford University Press, 1987. ISBN: 0198561814.

DUKLER, A. E., TAITEL, Y. "Flow Pattern Transitions in Gas-Liquid Systems: Measurement and Modeling". In: Hewitt, G. F., Delhaye, J. M., Zuber, N. (Eds.), *Multiphase Science and Technology: Volume 2*, Springer Berlin Heidelberg, pp. 1–94, Berlin, Heidelberg, 1986. ISBN: 978-3-662-01657-2.

DAVIES, R. M., TAYLOR, G. "The Mechanics of Large Bubbles Rising through Extended Liquids and through Liquids in Tubes", *Proceedings of the Royal Society*

of London Series A, v. 200, n. 1062, pp. 375–390, fev. 1950. doi: 10.1098/rspa.1950.0023.

MEHTA, B., KHANDEKAR, S. "Measurement of local heat transfer coefficient during gas–liquid Taylor bubble train flow by infra-red thermography", *International Journal of Heat and Fluid Flow*, v. 45, pp. 41–52, 2014. ISSN: 0142-727X. doi: https://doi.org/10.1016/j.ijheatfluidflow.2013.12.001. Disponível em: <https://www.sciencedirect.com/science/article/pii/S0142727X13002427>.

ETMINAN, A., MUZYCHKA, Y. S., POPE, K. "A Review on the Hydrodynamics of Taylor Flow in Microchannels: Experimental and Computational Studies", *Processes*, v. 9, n. 5, 2021. ISSN: 2227-9717. doi: 10.3390/pr9050870. Disponível em: <https://www.mdpi.com/2227-9717/9/5/870>.

WALSH, P. A., WALSH, E. J., MUZYCHKA, Y. S. "Heat transfer model for gas–liquid slug flows under constant flux", *International Journal of Heat and Mass Transfer*, v. 53, n. 15, pp. 3193–3201, 2010. ISSN: 0017-9310. doi: https://doi.org/10.1016/j.ijheatmasstransfer.2010.03.007. Disponível em: <https://www.sciencedirect.com/science/article/pii/S0017931010001407>.

CHO, S.-B., WANG, C., ALLEN, T., et al. "Review of Thermal-Hydraulic Modeling Methods of Printed Circuit Steam Generators for Small Modular Reactors". In: *ASME International Mechanical Engineering Congress and Exposition*, v. Volume 8: Fluids Engineering; Heat Transfer and Thermal Engineering, *ASME International Mechanical Engineering Congress and Exposition*, p. V008T11A058, 10 2022. doi: 10.1115/IMECE2022-96578. Disponível em: <https://doi.org/10.1115/IMECE2022-96578>.

KANG, H.-O., HAN, H., KIM, Y.-I. "Thermal-hydraulic Design of A Printed-Circuit Steam Generator for Integral Reactor", *Journal of Fluid Machinery*, v. 17, pp. 77–83, 12 2014. doi: 10.5293/kfma.2014.17.6.077.

BRETHERTON, F. P. "The motion of long bubbles in tubes", *Journal of Fluid Mechanics*, v. 10, n. 2, pp. 166–188, 1961. doi: 10.1017/S0022112061000160.

AUSSILLOUS, P., QUÉRÉ, D. "Quick deposition of a fluid on the wall of a tube", *Physics of Fluids - PHYS FLUIDS*, v. 12, pp. 2367–2371, 10 2000. doi: 10.1063/1.1289396.

HAN, Y., SHIKAZONO, N. "Measurement of the liquid film thickness in micro tube slug flow", *International Journal of Heat and Fluid Flow*, v. 30, n. 5, pp. 842–853, 2009. ISSN: 0142-727X. doi: https://doi.org/10.1016/j.ijheatfluidflow.2009.02.019. Disponível em: <https://www.sciencedirect.com/science/article/pii/S0142727X09000514>. The 3rd International Conference on Heat Transfer and Fluid Flow in Microscale.

WONG, H., RADKE, C. J., MORRIS, S. "The motion of long bubbles in polygonal capillaries. Part 1. Thin films", *Journal of Fluid Mechanics*, v. 292, pp. 71–94, 1995. doi: 10.1017/S0022112095001443.

MAGNINI, M. "Bubbles in capillaries: Relaxing traditional assumptions", *Science Talks*, v. 2, pp. 100020, 2022. ISSN: 2772-5693. doi: https://doi.org/10.1016/j.sctalk.2022.100020. Disponível em: <https://www.sciencedirect.com/science/article/pii/S2772569322000202>.

ZHANG, X., NIKOLAYEV, V. S. "Liquid film dynamics with immobile contact line during meniscus oscillation", *Journal of Fluid Mechanics*, v. 923, pp. A4, 2021. doi: 10.1017/jfm.2021.540.

ZHANG, X., NIKOLAYEV, V. S. "Dewetting acceleration by evaporation", *Journal of Fluid Mechanics*, v. 948, pp. A49, 2022. doi: 10.1017/jfm.2022.725.

WEATHERBURN, C. *Introduction to Riemannian Geometry and the Tensor Calculus.* Cambridge, Cambridge University Press, 1938.

MAGNINI, M., MUNICCHI, F., EL MELLAS, I., et al. "Liquid film distribution around long gas bubbles propagating in rectangular capillaries", *International Journal of Multiphase Flow*, v. 148, pp. 103939, 2022. ISSN: 0301-9322. doi: https://doi.org/10.1016/j.ijmultiphaseflow.2021.103939. Disponível em: <https://www.sciencedirect.com/science/article/pii/S0301932221003402>.

QUINTEN, M. "On the use of fast Fourier transform for optical layer thickness determination", *SN Applied Sciences*, v. 1, n. 8, jul 2019. doi: 10.1007/s42452-019-0866-9.

BRACKBILL, J., KOTHE, D., ZEMACH, C. "A continuum method for modeling surface tension", *Journal of Computational Physics*, v. 100, n. 2, pp. 335–354, 1992. ISSN: 0021-9991. doi: https://doi.org/10.1016/0021-9991(92)90240-Y. Disponível em: <https://www.sciencedirect.com/science/article/pii/002199919290240Y>.

Appendix A

Kinematic Boundary Condition at the Bubble Interface

At the gas-liquid interface, the kinematic boundary condition is given by

$$\mathbf{n} \cdot \tilde{\mathbf{u}} = 0, \tag{A.1}$$

where $\mathbf{n}$ is the unit normal vector at the interface, and $\tilde{\mathbf{u}}$ is the dimensionless fluid velocity.

This condition states that the normal component of the velocity at the interface must vanish. Physically, this means fluid particles on the bubble surface do not cross the interface; instead, the interface acts as a *stream surface*. In steady flow, the bubble boundary is material to the in-flowing liquid, and any motion of the interface occurs only tangentially. Mathematically, if the interface is defined as the zero level set of a function $F(\mathbf{x}, t) = 0$, then the kinematic condition follows from the fact that the velocity field is always tangent to the surface:

$$\frac{dF}{dt} = \frac{\partial F}{\partial t} + \mathbf{u} \cdot \nabla F = 0. \tag{A.2}$$

For steady bubble shapes in a moving reference frame, $\partial F/\partial t = 0$, so $\mathbf{u} \cdot \nabla F = 0$, confirming that flow at the interface is everywhere tangent to the surface.

Appendix B

Normal Stress Balance at the Bubble Interface

At the gas-liquid interface, the mechanical equilibrium in the normal direction requires that the total fluid stress balances the capillary force arising from surface tension and curvature. Mathematically, this is expressed as:

$$\boldsymbol{\tau} \cdot \mathbf{n} = \sigma \left(\nabla \cdot \mathbf{n} \right) \mathbf{n} \tag{B.1}$$

where $\boldsymbol{\tau}$ is the liquid stress tensor (inviscid gas), $\mathbf{n}$ is the unit normal to the interface, σ is the surface tension, and $\nabla \cdot \mathbf{n}$ is the mean curvature of the interface.

The left side represents the total force per unit area (including both pressure and viscous contributions) exerted by the liquid on the interface. The right side expresses the capillary force per unit area caused by surface tension acting on a curved interface (the Young–Laplace law). This boundary condition ensures that, at every point on the bubble surface, the local mechanical stress is balanced by the capillary pressure due to interfacial curvature.

Appendix C

Derivation of the interface profile equation in the lubrication limit

This appendix details the derivation of the third-order ordinary differential equation governing the interface profile in the film deposition region. The derivation proceeds from the Stokes momentum balance under lubrication assumptions and closes via capillarity and mass conservation.

Reference Frame and Assumptions

The analysis is performed in the reference frame moving with the bubble at velocity U. In this frame:

- The bubble shape and the local film thickness $h(x)$ are steady ($\partial/\partial t = 0$).
- The channel wall, located at $y = 0$, moves in the negative x-direction with velocity $-U$.
- The liquid film thickness h is much smaller than the channel transverse length scale ($h \ll a$).
- Interfacial slopes are small ($|dh/dx| \ll 1$), and inertial effects are negligible.

Axial Momentum Balance

Under these assumptions, the pressure p is uniform across the film thickness, and the axial momentum equation reduces to the Stokes balance:

$$\mu \frac{\partial^2 u}{\partial y^2} = \frac{dp}{dx} \tag{C.1}$$

where $u(x, y)$ is the axial velocity of the liquid. Since the pressure gradient depends only on the streamwise coordinate x, Eq. (C.1) can be integrated twice with respect to y:

$$u(x, y) = \frac{1}{2\mu} \frac{dp}{dx} y^2 + C_1(x) y + C_2(x) \tag{C.2}$$

Boundary Conditions

To determine the integration constants C_1 and C_2, we apply the physical boundary conditions appropriate for the bubble reference frame.

1. No-slip condition at the wall: At the solid wall ($y = 0$), the liquid moves with the wall velocity:

$$u(x, 0) = -U \quad \Longrightarrow \quad C_2(x) = -U \tag{C.3}$$

2. Zero tangential stress at the interface: At the gas-liquid interface ($y = h(x)$), the shear stress vanishes because the gas viscosity is negligible compared to that of the liquid:

$$\mu \left. \frac{\partial u}{\partial y} \right|_{y=h} = 0 \tag{C.4}$$

Differentiating Eq. (C.2) and applying this condition:

$$\frac{1}{\mu} \frac{dp}{dx} h + C_1 = 0 \quad \Longrightarrow \quad C_1(x) = -\frac{1}{\mu} \frac{dp}{dx} h \tag{C.5}$$

Substituting these constants back into Eq. (C.2) yields the parabolic velocity profile within the film:

$$u(x, y) = \frac{1}{2\mu} \frac{dp}{dx} (y^2 - 2hy) - U \tag{C.6}$$

Flux Conservation

We consider the volumetric flow rate per unit width, Q, flowing through the liquid film. Since the flow is steady in this reference frame, Q must be constant at any cross-section x.

$$Q = \int_0^h u(x, y)\, dy \tag{C.7}$$

Substituting Eq. (C.6) into the integral:

$$Q = \frac{1}{2\mu}\frac{dp}{dx}\left[\frac{y^3}{3} - hy^2\right]_0^h - [Uy]_0^h \tag{C.8}$$

$$Q = -\frac{h^3}{3\mu}\frac{dp}{dx} - Uh \tag{C.9}$$

To determine the value of the constant Q, we examine the flow far downstream (in the thin film region). Here, the film thickness becomes uniform ($h \to h_\infty$) and the pressure gradient vanishes ($dp/dx \to 0$). The liquid in this uniform film is carried solely by the moving wall (plug flow):

$$Q = -Uh_\infty \tag{C.10}$$

Equating the local flux (C.9) with the far-field flux (C.10):

$$-Uh_\infty = -\frac{h^3}{3\mu}\frac{dp}{dx} - Uh \tag{C.11}$$

Rearranging for the pressure gradient:

$$\frac{dp}{dx} = \frac{3\mu U}{h^3}(h_\infty - h) \tag{C.12}$$

Capillary Closure and Final Equation

The liquid pressure is related to the interfacial curvature κ by the Young-Laplace equation ($p = p_g - \sigma\kappa$). Assuming constant gas pressure and using the linearized curvature approximation for small slopes ($\kappa \approx d^2h/dx^2$):

$$\frac{dp}{dx} = -\sigma\frac{d\kappa}{dx} \approx -\sigma\frac{d^3h}{dx^3} \tag{C.13}$$

Finally, equating the viscous pressure gradient (C.12) with the capillary pressure gradient (C.13) yields the governing differential equation for the interface profile:

$$-\sigma\frac{d^3h}{dx^3} = \frac{3\mu U}{h^3}(h_\infty - h) \tag{C.14}$$

Or, rearranging to match the form presented in the main text:

$$\frac{d^3h}{dx^3} = \frac{3\mu U}{\sigma}\frac{h - h_\infty}{h^3} \tag{C.15}$$

This equation balances the capillary forces (LHS) with the viscous forces (RHS) and allows for the determination of the deposited film thickness h_∞ via asymptotic matching.

Role of the governing equation and subsequent scaling analysis. The lubrication equation derived above provides a quantitative description of the interface shape in the bubble reference frame, but it does not by itself determine the value of the asymptotic film thickness h_∞. This thickness enters the problem as an unknown parameter that must be selected through matching between the dynamic meniscus near the bubble front and the uniform thin film along the bubble body. Rather than solving the full nonlinear equation at this stage, insight into the selection mechanism and the associated length scales is obtained by a scaling analysis of the governing equation in the deposition region. This analysis identifies the dominant viscous–capillary balance and yields the characteristic scalings $h_\infty \sim a\,Ca^{2/3}$ and $\ell \sim a\,Ca^{1/3}$, which are then used to interpret the structure of the solution and the downstream relaxation of the interface.

Appendix D

Film deposition and downstream relaxation

In the film deposition region, viscous stresses generated by the relative motion between the bubble and the wall balance capillary pressure gradients arising from interfacial curvature variations. The analysis presented below clarifies how this balance determines both the axial extent of the deposition region and the asymptotic film thickness h_∞.

Lubrication framework. The analysis is carried out under the classical lubrication assumptions: the film thickness is much smaller than the channel transverse length scale ($h \ll a$), interfacial slopes are small ($|\partial h/\partial x| \ll 1$), inertial effects are negligible, and the flow is steady in the bubble reference frame. Under these conditions, the pressure is uniform across the film thickness and the axial momentum equation reduces at leading order to the Stokes balance

$$\frac{\partial p}{\partial x} = \mu \frac{\partial^2 u}{\partial y^2}, \tag{D.1}$$

where u is the axial velocity and p is the liquid pressure.

The axial velocity varies from zero at the bubble's interface to $O(U)$ at the wall across a film of thickness h. Consequently, the curvature of the velocity profile scales as

$$\frac{\partial^2 u}{\partial y^2} = O\left(\frac{U}{h^2}\right), \tag{D.2}$$

which implies that the streamwise pressure gradient induced by viscous stresses is

of order

$$\frac{\partial p}{\partial x} = O\left(\frac{\mu U}{h^2}\right). \tag{D.3}$$

Connection between interfacial curvature and pressure

The appearance of curvature in the pressure field originates from the Young–Laplace equation, which expresses the normal stress balance across a fluid–fluid interface. For a clean interface separating a gas phase (subscript g) and a liquid phase (subscript l), this balance reads

$$p_g - p_l = \sigma\kappa, \tag{D.4}$$

where σ is the surface tension and κ is the total mean curvature of the interface. In the present configuration, the gas viscosity is assumed negligible, so the gas pressure p_g may be taken as spatially uniform. As a result, spatial variations of the liquid pressure are entirely controlled by variations in the interfacial curvature,

$$\nabla p_l = -\sigma\nabla\kappa. \tag{D.5}$$

Decomposition of the curvature. The total curvature κ can be decomposed into contributions associated with the transverse and streamwise directions,

$$\kappa = \kappa_\perp + \kappa_x, \tag{D.6}$$

where $\kappa_\perp$ denotes the curvature imposed by the channel cross-sectional geometry and κ_x denotes the curvature associated with variations of the interface along the streamwise direction.

In the film deposition region, the transverse curvature is primarily set by the channel geometry and varies only weakly along x. Consequently, its streamwise gradient is negligible compared with that of the streamwise curvature,

$$\frac{\partial \kappa_\perp}{\partial x} \ll \frac{\partial \kappa_x}{\partial x}. \tag{D.7}$$

Therefore, only κ_x contributes at leading order to the streamwise pressure gradient.

Exact expression for the streamwise curvature. For an interface described by the height function $h(x)$, the exact geometric expression for the curvature in the streamwise plane is

$$\kappa_x = \frac{\partial^2 h/\partial x^2}{\left[1 + (\partial h/\partial x)^2\right]^{3/2}}. \tag{D.8}$$

Small-slope approximation. Within the lubrication regime, the interface slope is small,

$$\left|\frac{\partial h}{\partial x}\right| \ll 1, \tag{D.9}$$

which allows Eq. (D.8) to be expanded asymptotically. Retaining the leading-order term yields

$$\kappa_x \approx \frac{\partial^2 h}{\partial x^2}. \tag{D.10}$$

Higher-order corrections scale as $O((\partial h/\partial x)^2)$ and are therefore negligible at leading order.

Streamwise pressure gradient. Substituting Eq. (D.10) into Eq. (D.5) and differentiating along the streamwise direction yields

$$\frac{\partial p_l}{\partial x} = -\sigma \frac{\partial \kappa_x}{\partial x} \approx -\sigma \frac{\partial^3 h}{\partial x^3}. \tag{D.11}$$

This expression provides the capillary contribution to the streamwise pressure gradient appearing in the lubrication equation and justifies the emergence of the third-order derivative of the film thickness in the governing equation for the deposition region.

Viscous–capillary balance and governing equation. Equating the viscous contribution (D.3) and the capillary contribution (D.11) yields the leading-order lubrication equation governing the interface shape in the deposition region,

$$\sigma \frac{\partial^3 h}{\partial x^3} \sim \frac{\mu U}{h^2}. \tag{D.12}$$

This equation is not merely a scaling relation but represents the dominant balance in the governing differential equation for the film profile.

Extraction of characteristic scales. To interpret Eq. (D.12), characteristic scales are introduced. Let $h \sim h_\infty$ denote the deposited film thickness selected by the deposition process, and let $x \sim \ell$ denote the axial length scale over which the interface transitions from the curved rear meniscus to the uniform thin film. Under these definitions, the third derivative scales as

$$\frac{\partial^3 h}{\partial x^3} \sim \frac{h_\infty}{\ell^3}. \tag{D.13}$$

Substitution into Eq. (D.12) yields

$$\sigma \frac{h_\infty}{\ell^3} \sim \frac{\mu U}{h_\infty^2}. \tag{D.14}$$

Introducing the capillary number $Ca = \mu U/\sigma$, this balance reduces to

$$h_\infty^3 \sim Ca\, \ell^3. \tag{D.15}$$

Geometric matching with the static meniscus. A second independent relation follows from geometric matching. Upstream of the deposition region, the interface coincides with a static meniscus whose streamwise curvature is set by the channel size,

$$\kappa_x \sim \frac{1}{a}. \tag{D.16}$$

Within the deposition region, the streamwise curvature associated with the evolving film profile scales as

$$\kappa_x \sim \frac{\partial^2 h}{\partial x^2} \sim \frac{h_\infty}{\ell^2}. \tag{D.17}$$

Requiring a smooth asymptotic matching between the static meniscus and the deposited film therefore implies

$$\frac{h_\infty}{\ell^2} \sim \frac{1}{a}. \tag{D.18}$$

Determination of the Bretherton scalings. Solving Eqs. (D.15) and (D.18) simultaneously yields

$$\ell \sim a\, Ca^{1/3}, \qquad h_\infty \sim a\, Ca^{2/3}. \tag{D.19}$$

Thus, the axial extent of the deposition region scales as $aCa^{1/3}$, while the deposited film thickness scales as $aCa^{2/3}$, in agreement with the classical Bretherton result.

Downstream relaxation toward the uniform film. Downstream of the deposition region, the film thickness approaches its asymptotic value h_∞. Writing the film profile as

$$h(x) = h_\infty + \delta h(x), \qquad |\delta h| \ll h_\infty, \tag{D.20}$$

and substituting this expression into Eq. (D.12), the nonlinear term $1/h^2$ can be linearized about h_∞. This procedure yields a linear, constant-coefficient differential equation governing δh, whose solutions decay exponentially with downstream distance. The characteristic decay length is set by the deposition length scale $\ell \sim aCa^{1/3}$.

Downstream linear relaxation. Write the film profile as a small perturbation about the uniform film,

$$h(x) = h_\infty + \delta h(x), \qquad |\delta h| \ll h_\infty,$$

and substitute into the lubrication equation

$$\sigma \frac{d^3 h}{dx^3} = \frac{3\mu U}{h^3}\,(h_\infty - h).$$

Linearizing about h_∞ (i.e. replacing h^{-3} by h_∞^{-3} and retaining only terms linear in δh) yields the constant-coefficient ODE

$$\sigma \frac{d^3 \delta h}{dx^3} \;=\; -\frac{3\mu U}{h_\infty^3}\,\delta h.$$

Setting $k \equiv 3\mu U/h_\infty^3 > 0$, the characteristic equation is

$$r^3 + \frac{k}{\sigma} = 0,$$

whose three roots are

$$r_n = \left(\frac{k}{\sigma}\right)^{1/3} e^{i(\pi+2\pi n)/3}, \qquad n = 0, 1, 2.$$

One root is real and negative,

$$r_{\mathrm{real}} = -\left(\tfrac{k}{\sigma}\right)^{1/3},$$

while the other two are complex with positive real part. For x measured downstream from the meniscus the requirement that the disturbance remain bounded as $x \to +\infty$ forces the two growing/oscillatory modes to be absent; the far-field behaviour is therefore governed by the single decaying mode:

$$\delta h(x) = A\,\exp\!\big(r_{\mathrm{real}}\,x\big) + \cdots = A \exp\!\Big(-\frac{x}{\lambda}\Big) + \cdots\,,$$

with the characteristic decay length

$$\lambda \;=\; \Big(\frac{\sigma}{k}\Big)^{1/3} \;=\; \Big(\frac{\sigma h_\infty^3}{3\mu U}\Big)^{1/3}.$$

Using $h_\infty = O(a\,Ca^{2/3})$ and $\mu U = \sigma Ca$ gives $\lambda = O(a\,Ca^{1/3})$ (more precisely $\lambda \approx a\,Ca^{1/3}/3^{1/3}$). Hence, asymptotically downstream

$$h(x) = h_\infty + O\big(h_\infty\,\exp\!\big(-x/\lambda\big)\big)\,,$$

showing that residual curvature decays exponentially over the deposition length scale $\lambda \sim a\,Ca^{1/3}$.